Research Square

Preprints are preliminary reports that have not undergone peer review.
They should not be considered conclusive, used to inform clinical practice,
or referenced by the media as validated information.

# Multiscale Phenomics Reveals a Varietal Signature of Grapevine Response to Heatwaves

**Kidanemaryam Reta**
Ben-Gurion University of the Negev
**Tamir Caras**
Ben-Gurion University of the Negev
**Pankaj Kumar Verma**
Ben-Gurion University of the Negev
**Noga Sikon-Persi**
Ben-Gurion University of the Negev
**Nang Cherry**
Ben-Gurion University of the Negev
**Amnon Bustan**
Ramat Negev Desert Agro-Research Center
**Naftali Lazarovitch**
Ben-Gurion University of the Negev
**Tarin Paz-Kagan**
Ben-Gurion University of the Negev
**Aaron Fait**
fait@bgu.ac.il

Ben-Gurion University of the Negev

**Article**

**Keywords:** Vitis vinifera, abiotic stress, plant physiology, network analysis, metabolomics, thermal sensing, temperature

**Posted Date:** July 22nd, 2026

**DOI:** https://doi.org/10.21203/rs.3.rs-10256443/v1

**License:** This work is licensed under a Creative Commons Attribution 4.0 International License.
Read Full License

**Additional Declarations:** No competing interests reported.

**Multiscale Phenomics Reveals a Varietal Signature of Grapevine Response to Heatwaves**

Kidanemaryam Reta[1,2], Tamir Caras[3], Pankaj Kumar Verma[1], Noga Sikron Persi[2], Nang Cherry[1], Amnon Bustan[4], Naftali Lazarovitch[5], Tarin Paz-Kagan[3], Aaron Fait*[2]

**Corresponding author**: Aaron Fait, E-mail: fait@bgu.ac.il

[1]Albert Katz International School for Desert Studies, Jacob Blaustein Institutes for Desert Research, Ben-Gurion University of the Negev, Sede-Boqer Campus, 849900 Israel
[2]Albert Katz Department of Dryland Biotechnologies, French Associates Institute for Agriculture and Biotechnology of Drylands, Jacob Blaustein Institutes for Desert Research, Ben-Gurion University of the Negev, Sede-Boqer Campus, 849900 Israel
[3]French Associates Institute for Agriculture and Biotechnology of Drylands, The Jacob Blaustein Institutes for Desert Research, Ben-Gurion University of the Negev, Sede-Boqer Campus, 849900, Israel
[4]Ramat Negev Desert Agro-Research Center, Ramat Negev, Halutza 851900, Israel
[5]Wyler Department for Dryland Agriculture, French Associates Institute for Agriculture and Biotechnology of Drylands, Jacob Blaustein Institutes for Desert Research, Ben-Gurion University of the Negev, Sede-Boqer Campus, 849900 Israel

**Abstract**

**Background**. Climate change increasingly threatens viticulture, with Mediterranean wine regions expected to face more frequent and intense heatwaves. Identifying grapevine varieties with superior heat resilience is therefore critical for sustainable production in arid and semi-arid environments.

**Methods**. We applied an integrative phenotyping framework combining leaf physiology, metabolomics, targeted gene expression profiling, and UAV-based thermal imaging to characterize heatwave responses in six *Vitis vinifera* varieties over three growing seasons (2022–2024).

**Results**. Marked varietal differences were observed across physiological, thermal, and molecular levels. Syrah maintained higher stomatal conductance (0.6 mol $m^{-2}$ $s^{-1}$) and net $CO_2$ assimilation rates (27 μmol $m^{-2}$ $s^{-1}$) under heat stress, compared to more sensitive varieties such as Tempranillo. This was accompanied by cooler canopy temperatures captured by UAV thermal imaging, validating its utility for rapid field-scale phenotyping. While interannual variations reflected local climatic fluctuations during each heatwave event, tolerant varieties consistently maintained higher quantum yields and electron transport capacities across all years. Metabolite profiling revealed that amino acids, sugars, and polyols served as major components of heat adaptation, with distinct metabolic shifts discriminating between temporal stress responses. Targeted gene-expression profiling identified variety-specific regulation of heat-shock protein and sugar transport pathways, highlighting *HT4* as a potential regulator of thermotolerance.

Furthermore, correlation-network analysis revealed that resilient varieties exhibited tighter coordination between molecular and physiological responses.

**Conclusion**. Together, these findings reveal substantial varietal diversity in grapevine heat-response strategies. Integrating UAV-based phenotyping with broad molecular profiling can provide a scalable framework for screening climate-resilient cultivars and guiding adaptation strategies in future viticulture.

**Keywords**: *Vitis vinifera*, abiotic stress, plant physiology, network analysis, metabolomics, thermal sensing, temperature

## 1. Introduction

Grapevine (*Vitis vinifera* L.) is an economically important crop currently facing intensifying threats from climate change (van Leeuwen et al., 2024), driven by rising temperatures and extreme weather events like heatwaves and droughts (IPCC, 2023). These stresses are particularly acute in semi-arid to arid Mediterranean regions (Mozell and Thach, 2014), where they jeopardize the long-term sustainability of viticulture. Globally, grape production reached 78.21 million tons spanning across 7.3 million hectares in 2022 (FAOSTAT, 2023), with wine production at 258 million hectoliters (OIV, 2023). However, compounded climate extremes have drastically impacted recent yields, causing global wine production to decline to 244.1 million hectoliters in 2023 and further plummeting to a 60-year low of 232 million hectoliters in 2024 (OIV, 2025). This steep decline underscores the acute vulnerability of viticultural systems to elevated thermal stress. At the vine level, heat stress severely compromises physiological and agronomic performance, degrades berry quality, alters wine composition, and drives up irrigation dependency (Guo et al., 2016). Elevated temperatures alter phenology and disrupt both primary and secondary metabolism (Gashu et al., 2022). Extreme heatwaves are defined as periods of three or more consecutive days exceeding 35 °C that exert profound effects on fruits by inhibiting fruit sugar transport and accumulation (Gambetta et al., 2021), shifting critical phenological stages, and increasing the risk of yield loss through sunburns, berry shriveling, and fruit rot (Bernardo et al., 2018).

At the organismal level, the grapevine physiological response to severe heat stress involves intricate, coordinated alterations in gas exchange and photosynthetic efficiency (Flexas et al., 2010). To mitigate excessive transpirational water loss, grapevines restrict stomatal conductance, though this compromises $CO_2$ uptake and net assimilation capacity (Medrano et al., 2002). Within the photosynthetic apparatus, Photosystem II (PSII) is particularly heat-sensitive; heat-induced damage to PSII triggers photoinhibition, which depresses electron transport rates and the maximum quantum efficiency (Berry and Björkman, 1980; Mathur et al., 2014). Consequently, chlorophyll fluorescence parameters, specifically the effective quantum yield of PSII (PhiPS2[$\Phi_{PSII}$]), electron transport rate (ETR), and non-photochemical quenching (NPQ), serve as robust, non-destructive indicators for early stress detection and the comparative assessment of

varietal thermotolerance (Havaux, 1998; Maxwell and Johnson, 2000; Salvucci and Crafts-Brandner, 2004). Crucially, heat-tolerant genotypes are distinguished by higher $\Phi_{PSII}$ values and execute more efficient NPQ transitions under severe thermal loads, demonstrating superior functional resilience of their photosynthetic machinery (Greer and Weedon, 2012).

Beyond physical gas exchange, thermal stress also triggers systematic metabolic readjustment across the whole plant (Obata and Fernie, 2012; Rienth et al., 2016). In grapevine, the metabolic status of the leaves exerts a direct influence on berry composition and final wine quality (Dai et al., 2011). Primary metabolites, including sugars, free amino acids, and tricarboxylic acid (TCA) cycle intermediates, serve as the functional core of stress tolerance while simultaneously providing precursors that shape complex secondary metabolite profiles. To maintain cellular osmotic potential and stabilize protein structure, grapevines rapidly accumulate a wide range of compatible solutes, including proline, glycine betaine, and polyols (Krasensky and Jonak, 2012; Zhao et al., 2016; Guo et al., 2017). High-resolution metabolomic profiling has uncovered substantial varietal divergence in these pathways, with time-course analyses revealing variety-specific metabolic signatures (Pastore et al., 2017; Gashu et al., 2020; Pettenuzzo et al., 2022; Guo et al., 2025; Martínez-Lüscher et al., 2025). While certain cultivars rely on highly reactive stress-induced synthesis of protective compounds, others favor maintaining elevated constitutive levels of baseline protectants (Krasensky and Jonak, 2012; Carvalho et al., 2015). Deciphering these underlying metabolic signatures is therefore imperative for tailoring targeted breeding programs and vineyard management strategies to sustain a climate-resilient viticulture.

At the molecular level, genes governing antioxidant defense, osmotic adjustment, and membrane stabilization are coordinately regulated to enhance cellular thermotolerance (Kotak et al., 2007; Mittler et al., 2012; Torregrosa et al., 2017). Despite these insights, the exact molecular mechanisms governing carbon partitioning between source leaves and developing fruit (sinks) under acute thermal stress, and how these dynamics vary across diverse genetic backgrounds, remain poorly understood.

Because stomatal regulation, transpiration, and photosynthetic impairment directly influence leaf energy balance, these physiological responses are reflected in changes in canopy temperature. Consequently, high-resolution thermal imaging has emerged as a robust, non-destructive tool for monitoring plant temperature dynamics, linking underlying biochemical processes to field-level phenotypes (Awais et al., 2023; Kundu et al., 2024; Liang et al., 2025; Sharma et al., 2026). Unmanned Aerial Vehicle (UAV)-based platforms have revolutionized field-scale viticulture phenotyping by providing the spatial and temporal resolution necessary to capture per-plant water status and canopy conductance variations across entire vineyards (Zarco-Tejada et al., 2013; Bellvert et al., 2014). While UAV-derived thermal indices correlate strongly with ground-based physiological parameters, these aerial estimates remain highly sensitive to sensor drift, viewing geometries, and rapid environmental fluctuations (Treier et al., 2025). Overcoming these

challenges requires rigorous calibration and multi-season validation to ensure reliable biological interpretation during acute thermal shocks.

Although multi-omics frameworks combining molecular, metabolic, and physiological data have significantly advanced plant stress research, their application remains largely confined to controlled environments or fails to integrate with field-scale phenotyping (Ćavar Zeljković et al., 2026). In fact, bridging UAV-based high-throughput field phenotyping with deep multi-omics datasets remains exceptionally rare; most studies either focus strictly on omics integration or link genomic data with image-based traits, thereby failing to capture dynamic metabolic and transcriptional shifts under actual field conditions. While recent advances in predictive crop modeling highlight the immense potential of multi-scale integration (Cembrowska-Lech et al., 2023), a critical knowledge gap persists in directly linking canopy-scale UAV thermal phenotypes with underlying molecular and metabolic regulation during heatwaves. Crucially, this gap is widened by a lack of research evaluating how these multi-scale mechanisms vary across different genetic backgrounds, as characterizing genotypic diversity is essential to uncovering distinct varietal coping strategies (Gashu et al., 2020; Burgess, 2022; Villano et al., 2022; Wegher et al., 2025). Successfully operationalizing such a comprehensive, multi-variety platform demands robust analytical workflows, multi-year validation, and precise interdisciplinary integration (Araus and Cairns, 2014; Fahlgren et al., 2015; Tardieu et al., 2017). However, previous studies have primarily focused on broad shifts in phenology, yield, or berry composition, while giving limited attention to the integrated biological mechanisms that govern varietal resilience to acute heat stress (Wolkovich et al., 2018; van Leeuwen et al., 2024).

Consequently, it remains unclear how grapevine varieties coordinate responses across multiple biological levels, from canopy thermal regulation and gas exchange to metabolic reprogramming and gene regulation. In addition, only a handful of studies have linked high-throughput remote-sensing phenotypes to molecular and physiological traits under operational vineyard conditions (Gago et al., 2017; Alahmad et al., 2025). Here, we used an integrative phenotyping framework that combined UAV-based thermal remote sensing, plant physiology (gas exchange and fluorometry) measurements, metabolomics, and targeted gene expression analysis across multiple commercial grapevine varieties during natural seasonal heatwaves in the arid region of Southern Israel. Specifically, our approach aimed to (1) identify physiological, metabolic, and transcriptional responses associated with heat-induced changes in grapevine leaves, (2) associate plant molecular physiology with UAV thermal phenotypes, and (3) identify potential markers for the development of swift response strategies in the field.

## 2. Materials and Methods

### 2.1. Study area and experimental design

The experiment was conducted during consecutive growing seasons between 2022 and 2024 in an experimental vineyard (Fig. 1c) located at the Ramat Negev Desert Agro-Research Center

(30°58′43.4″ N, 34°42′31.6″ E, 300 m above sea level). The region features a hyperarid, desert-fringe climate characterized by very low rainfall (~80 mm annually between November and April) and negligible precipitation during the growing season. The vineyard experiences intense daytime solar radiation (600–1,100 W $m^{-2}$ between 09:00 and 15:00), extremely low relative humidity, and stark diurnal temperature fluctuations, with maximum summer air temperatures regularly exceeding 30 °C. Continuous microclimatic monitoring was maintained via an automated on-site weather station that recorded air temperature, relative humidity, solar irradiance, and wind speed at 10-minute intervals. These environmental datasets were integrated directly with the plant physiological data.

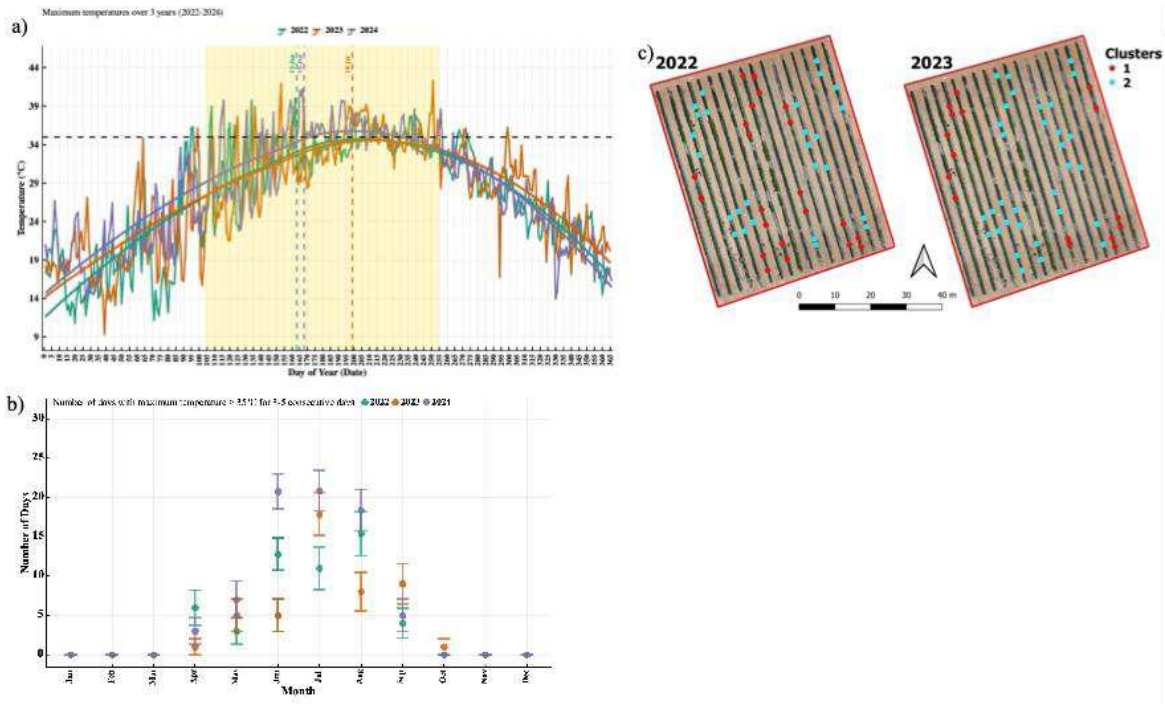



Figure 1: The maximum temperature of the years during the experimentation time. (a) Range of maximum temperatures recorded over 3 years, with vertical lines indicating days on which sampling and measurements were carried out, and the curved lines indicate the range of maximum temperature, and (b) number of heatwave days over 8 years, defined as ≥3 consecutive days with maximum air temperature >35 °C. (c) UAV-captured aerial view of the experimental vineyard along thermal image-derived canopy temperature profiles for each grapevine variety.

2.2. Plant material and experimental vineyard management

The study evaluated six commercial red wine grape (*Vitis vinifera*) cultivars: Syrah, Petite Sirah, Petit Verdot, Pinot Noir, Sangiovese, and Tempranillo. All cultivars were grafted onto 140 Ruggeri (140 RU) rootstock and established in 2012 on sandy-loam soil under controlled drip irrigation. Vines were planted at a density of 3 × 1.5 m, oriented North-to-South, and trained to a vertical shoot position (VSP) trellis system with a maximum canopy height limited to 2 m. The vineyard

layout followed a randomized complete block design (RCBD) consisting of four biological replicates, with each plot containing eight to nine vines per cultivar.

Drip irrigation was scheduled weekly based on potential evapotranspiration ($ET_0$) calculations, delivering approximately 500 mm of water annually from bloom to harvest. Rows were managed using white plastic mulch to suppress evaporation. Controlled deficit irrigation was applied using a crop coefficient ($K_c$) of ~0.35 before véraison, which was reduced to ~0.25 post-véraison to maintain a standardized, moderate water deficit across all varieties. Nutrients were uniformly supplied via fertigation, and diseases or pests were controlled in accordance with regional integrated pest management (IPM) protocols. Winter pruning, along with cluster and shoot thinning, was practiced annually to regulate crop load to a target yield of 10–15 Mg $ha^{-1}$. This highly standardized management framework minimized agronomic confounding factors, isolating the distinct physiological responses of the cultivars to thermal stress.

2.3. Heatwave characterization and diurnal sampling protocols

Field measurements and tissue sampling were conducted during naturally occurring heatwaves. A heatwave was defined as a period of 3–5 consecutive days where daily maximum air temperatures exceeded 35 °C (Fig. 1a-c). To characterize acute midday thermal stress and diurnal recovery dynamics, data were collected repeatedly during each heatwave at three key diurnal intervals: morning, noon, and evening. This high-frequency sampling framework captured plant physiological responses at peak daily temperatures alongside short-term recovery patterns under hyper-arid field conditions.

2.4. Leaf sampling and diurnal timeline.

To assess metabolic and molecular shifts under thermal stress, leaf samples were collected on June 12, 2022, July 18, 2023, and June 16, 2024. Each sampling campaign was executed following 3–5 consecutive days of a naturally occurring heatwave exceeding 35 °C (Fig. 1a, b). For each cultivar, fully expanded, sun-exposed leaves were collected at three distinct diurnal intervals to monitor variations in stress and recovery dynamics: morning (07:00), noon (12:00), and evening (16:00). At each time point, eight biological replicates were sampled per cultivar, totaling 144 leaf samples per campaign (6 cultivars × 3 timepoints × 8 replicates). Fresh leaf tissues were immediately flash-frozen in liquid nitrogen in the field to stop metabolic activity and preserve molecular integrity, and stored at −80 °C until metabolite profiling and gene expression analyses.

2.5. In situ leaf gas exchange measurements

Concurrently with leaf sampling, leaf gas exchange and fluorometry parameters were recorded using a LI-6800 portable photosynthesis system (LI-COR Biosciences, Lincoln, NE, USA). Measurements were taken on the youngest, fully expanded, sun-exposed leaf from the identical vines used for tissue sampling. Monitored parameters included net photosynthetic assimilation rate ($A$), transpiration rate ($E$), stomatal conductance ($g_s$), and intercellular $CO_2$ concentration ($C_i$). At the same time, chlorophyll fluorescence traits were measured, including electron transport rate

(ETR), non-photochemical quenching (NPQ), and effective quantum yield of photosystem II ($\Phi_{PSII}$). Chamber conditions were standardized with a $CO_2$ concentration of 400 ppm and an air flow rate of 500 μmol $s^{-1}$. Light intensity inside the chamber was set to 2,000 μmol $m^{-2}$ $s^{-1}$ using the integrated fluorometer light source, matching or exceeding ambient saturating light conditions. To capture realistic field-stress responses, the LI-6800 block temperature was dynamically adjusted at each diurnal interval to mirror the prevailing ambient air temperature gradient. Infrared gas analyzers (IRGAs) were matched every 10 minutes throughout each measurement window to eliminate instrumental drift.

### 2.6. UAV-based thermal imagery acquisition

Unmanned aerial vehicle (UAV) remote sensing campaigns were deployed concurrently with ground-based physiological and tissue sampling. Flights were executed three times daily at 08:00, 12:00, and 16:00 to align with morning, peak midday, and afternoon recovery phases. UAV operations were maintained at a flight altitude of 25 m above ground level (AGL) (Garcia-Garcia et al., 2021). To accommodate hardware updates across the multi-year study, two separate radiometric thermal platforms were utilized. On June 12, 2022, imagery was captured using a DJI Mavic 2 Enterprise Advanced featuring an integrated uncooled radiometric microbolometer (spectral range: 8–14 μm; resolution: 640 × 512 pixels; pixel pitch: 12 μm). On July 18, 2023**,** and June 16, 2024, flights utilized a DJI Matrice 300 RTK equipped with a DJI Zenmuse H20T thermal sensor, which shared identical core technical resolution and spectral specifications but offered enhanced operational stability. Both thermal sensors possess a factory-certified measurement accuracy of ±2 °C or ±2% of the reading. Potential interannual calibration bias from the sensor transition was mitigated by standardizing all orthomosaic processing pipelines, normalizing canopy temperatures against ambient weather station data, and focusing downstream interpretations on relative intra-cultivar rankings and diurnal response trajectories rather than raw, uncorrected absolute values.

#### 2.6.1 Thermal image processing and canopy temperature extraction

Thermal imagery captured by both UAV sensors was recorded as digital numbers (DN) and converted to absolute temperature values (°C) using a standardized computational pipeline. Radiometric temperature maps were generated using a custom R (v4.3.1) (R Core Team, 2024) script that interfaced directly with the DJI Thermal SDK (v1.4). Input parameters for the radiometric correction model, including atmospheric temperature and relative humidity, were retrieved from the corresponding 10-minute intervals of the on-site meteorological station. For each flight campaign, individual thermal frames were stitched into georeferenced orthomosaics and co-registered to a master spatial template to ensure precise spatial alignment across the diurnal time series. A single flight dataset (June 12, 2022, at 12:00) exhibited a systematic calibration offset and was adjusted using concurrent ambient temperature references and known stable ground targets prior to downstream analysis.

Representative canopy temperature ($T_c$) was extracted by averaging pixels within a 50-cm-diameter circular region of interest (ROI) centered on the coordinate of each ground-monitored vine crown. To eliminate confounding artifacts from sensor transitions, seasonal background divergence, and macroclimatic differences between years, downstream analyses focused strictly on within-day temperature dynamics (morning-to-noon and noon-to-evening differentials). Canopy temperature was normalized against concurrent ambient air temperature ($T_a$) to calculate the crop-ambient temperature differential ($\Delta T = T_c - T_a$). The diurnal variations in $\Delta T$ were then used to quantify canopy heating and cooling dynamics during acute heatwave events, which were interpreted in conjunction with in situ physiological parameters to characterize cultivar-specific thermoregulation patterns (Katimbo et al., 2022).

2.6.2. UAV-derived data analysis, clustering, and integration

Statistical evaluation of the UAV-derived thermal data comprised two complementary analytical streams: (i) the quantification of diurnal canopy thermal dynamics across distinct heatwave campaigns, and (ii) the classification of cultivar-specific thermoregulatory strategies using unsupervised machine learning. To evaluate macroclimatic variations between campaign years without the confounding effects of absolute temperature baselines, diurnal canopy temperature differentials ($\Delta T$) were calculated within each campaign day across two discrete temporal intervals: morning-to-noon ($\Delta T_{morning–noon}$) and noon-to-evening ($\Delta T_{\text{noon–evening}}$). Interannual variations in these within-day thermal trajectories were assessed using a two-sided Wilcoxon rank-sum test (Mann–Whitney $U$ test). For this macroclimatic comparison, data were pooled across all cultivars ($n$ = 48 observations per flight per year) to exclude cultivar identity from the primary inference framework. Significance values were adjusted using a Bonferroni correction to control the family-wise error rate across the multiple interval comparisons.

To isolate and characterize distinct varietal thermal response strategies, individual vine datasets were grouped using an unsupervised clustering framework. Prior to analysis, replicate values were aggregated and averaged at the individual-vine level to eliminate spatial pseudo-replication and ensure equal weighting within the model. The optimal number of partitions was determined mathematically using the Calinski–Harabasz variance ratio criterion (Caliński and Harabasz, 1974). Subsequently, a fuzzy $C$-means (FCM) clustering algorithm was deployed to assign each vine a continuous, probabilistic membership vector across the identified clusters (Bezdek et al., 1984). The resulting clusters were interpreted as distinct, empirical thermal response phenotypes that describe variations in canopy heating and cooling dynamics, rather than predefined, rigid tolerance categories.

All geospatial processing and orthomosaic manipulations were executed in QGIS (v3.22.14) (QGIS Development Team, 2021). All downstream statistical modeling, unsupervised machine learning, and non-parametric tests were performed within the R statistical computing environment (v4.3.1) (R Core Team, 2024).

2.7. Extraction, derivatization, and GC-MS profiling of primary metabolites

Frozen leaf tissue samples were lyophilized using a freeze dryer (ScanVac CoolSafe; LaboGene, Lillerød, Denmark) and homogenized into a fine powder at 25 Hz for 2 min using a pre-cooled mixer mill (MM 400; Retsch, Haan, Germany). Polar primary metabolites were extracted using a modified phase-separation protocol (Lisec et al., 2006) as described previously (Degu et al., 2014; Reta et al., 2025, 2026). Aliquots of 50 mg of lyophilized tissue powder were mixed with 1 mL of a pre-cooled extraction solvent mixture containing chloroform, methanol, and water (2.5:1:1, *v/v/v*). The extraction solvent was supplemented with 0.2 mg $mL^{-1}$ of $^{13}C_6$-sorbitol as an internal standard for retention-time and recovery normalization. The tissue-solvent mixtures were sequentially subjected to vortexing (Microspin FV-2400; Biosan, Riga, Latvia), incubation in an orbital thermoshaker (PHMT Thermoshaker; Grant-Bio, Shepreth, UK) at 25 °C and 1,000 rpm for 10 min, sonication at room temperature for 10 min, and centrifugation at 20,800 *g* for 10 min at 4 °C (Centrifuge 5417 R; Eppendorf, Hamburg, Germany). Phase separation was induced by adding chloroform and water, followed by a final centrifugation step. To ensure rigorous quality control and monitor instrument drift, a 50 µL aliquot from each sample supernatant was pooled to generate a composite quality control (QC) reference. Aliquots of 200 µL from each sample and the pooled QC were concentrated using a vacuum concentrator (Concentrator plus; Eppendorf, Hamburg, Germany).

Dried extract residues were derivatized via a two-step chemical protocol (Lisec et al., 2006; Reta et al., 2025). Methoximation was initiated by adding 40 µL of methoxyamine hydrochloride solution and incubating the mixtures at 37 °C for 2 h in a thermoshaker. Trimethylsilylation was subsequently performed by adding 70 µL of *N*-methyl-*N*-(trimethylsilyl)trifluoroacetamide (MSTFA) and 7 µL of a retention index alkane standard mixture ($C_{10}$–$C_{32}$), followed by agitation at 37 °C for 30 min. Derivatized solutions were transferred to glass chromatography vial inserts for automated injection.

Gas chromatography-mass spectrometry (GC-MS) analysis was performed on an integrated Agilent system comprising a 7693 automated liquid sampler, a 7890B gas chromatograph, and a 5977B mass-selective detector (Agilent Technologies, Santa Clara, CA, USA). Chromatographic separation was achieved on a VF-5ms capillary column (30 m length × 0.25 mm internal diameter × 0.25 µm film thickness) equipped with a 10-m EZ-Guard pre-column (Agilent Technologies). The oven temperature program was initiated at 70 °C and ramped to a final temperature of 340 °C using variable ramp rates as previously defined (Reta et al., 2025, 2026). Electron ionization mass spectra were acquired at a scan rate of 1.6 scans $s^{-1}$ over a mass-to-charge ratio range of 50–550 *m/z*. Primary metabolite annotation and peak integration were performed using MassHunter Workstation software (v10.0) (Agilent Technologies, Santa Clara, CA, USA) by matching mass fragmentation spectra against the National Institute of Standards and Technology (NIST) library and the Retention Index (RI) database from the Max Planck Institute for Molecular Plant Physiology (Golm, Germany). Quantified metabolite intensities were normalized against the

internal standard and batch-corrected using the pooled QC technical replicates to mitigate instrumental variation.

2.8. Total RNA extraction, purification, and cDNA synthesis

Total RNA was extracted from frozen leaf tissue using a modified cetyltrimethylammonium bromide (CTAB) protocol optimized for tissues rich in polyphenols and polysaccharides (Gambino et al., 2008). Aliquots of approximately 100–120 mg of tissue powder, homogenized using a liquid nitrogen-chilled mortar and pestle, were transferred to tubes containing 700 µL of CTAB extraction buffer supplemented with 2% (*v/v*) β-mercaptoethanol. The mixtures were incubated on ice for 5 min with periodic inversion to facilitate cell lysis.

Following incubation, the homogenates were centrifuged at 20,800 *g* for 5 min at 4 °C (Centrifuge 5417 R; Eppendorf, Hamburg, Germany). The resulting supernatant (~600–650 µL) was transferred to a clean tube, mixed thoroughly with an equal volume of chloroform to separate proteins and lipids, and centrifuged at 20,800 *g* for 5 min at 4 °C. The upper aqueous phase was isolated, and RNA precipitation was induced by adding an equal volume of ice-cold isopropanol. The precipitate was pelleted via centrifugation at 20,800 g for 20 min at 4 °C. The RNA pellet was washed with 500 µL of ice-cold 70% *v/v* ethanol, centrifuged at 20,800 *g* for 5 min at 4 °C, and air-dried at room temperature to eliminate residual ethanol.

To eliminate potential genomic DNA contamination, the dried pellet was resuspended in 85 µL of RNase-free water and treated with 5 µL of Dnase in 10 µL of DNA Digestion Buffer (Zymo Research, Irvine, CA, USA) at room temperature for 30 min. Following digestion, the reaction volume was adjusted with 200 µL of RNase-free water and 200 µL of chloroform, mixed vigorously, and centrifuged at 20,800 g for 2 min. The upper aqueous phase (~290 µL) was recovered, and RNA was selectively reprecipitated by adding a 1/3 volume (100 µL) of 7.5 M LiCl. The mixture was incubated at −20 °C for at least 20 min, then centrifuged at 20,800 g for 30 min at 4 °C. The purified RNA pellet was washed twice with 500 µL of ice-cold 70% *v/v* ethanol and air-dried.

The final RNA pellet was dissolved in 25 µL of RNase-free water for 15 min at 4 °C, followed by centrifugation at 20,800 *g* for 2 min to remove insoluble debris. RNA concentration and purity were assessed using a NanoDrop 1000 spectrophotometer (v3.8.1) (Thermo Fisher Scientific, Waltham, MA, USA) based on absorbance ratios at $A_{260}/A_{280}$ (for protein contamination) and $A_{260}/A_{230}$ (for organic/polysaccharide contamination). For downstream transcriptional analysis, 1 µg of high-quality total RNA was reverse-transcribed into complementary DNA (cDNA) using the qScript cDNA Synthesis Kit (QuantaBio, Beverly, MA, USA) according to the manufacturer's instructions. Extracted RNA and cDNA templates were stored at −80 °C until quantitative polymerase chain reaction (qPCR) amplification.

2.9. Primer design and quantitative Real-Time PCR (qRT-PCR) expression analysis

Gene-specific primers for target transcripts were designed using the NCBI Primer-BLAST tool (Ye et al., 2012). Amplification efficiency for each primer pair was empirically evaluated using standard curves generated from serial dilutions of a pooled cDNA template. To quantify target gene expression profiles under heatwave conditions, real-time PCR was performed using Power SYBR Green PCR Master Mix (Applied Biosystems, Foster City, CA, USA) on a real-time thermal cycler, according to the manufacturer's protocols.

Prior to amplification, cDNA templates were diluted 1:100 (*v/v*) in RNase-free water. Relative transcript abundance was calculated using the comparative cycle threshold ($2^{-\Delta\Delta C_T}$) method. Target gene expression values were normalized against the internal reference housekeeping gene *Ubiquitin 1* (*VvUBQ1*) to control for technical variations in initial template concentration. The experimental setup comprised four biological replicates per cultivar and timepoint, with each sample analyzed in three technical replicates to ensure analytical reproducibility.

2.10. Statistical analysis

The statistical analyses and visualizations were conducted using R version 4.5.1 (R Core Team, 2025) within RStudio IDE version 2025.05.1 build 513 (Posit team, 2025). To investigate the impact of the heatwave on the leaves' physiological activities and metabolic levels, a three-way ANOVA for combined analysis and a two-way ANOVA for single-year repeated-measures were applied to explore the effect of the heatwave across time points using the built-in "*Anova*" and "*lm*" functions. A hierarchically clustered complex heatmap with side annotations was generated based on log2-transformed values of metabolic relative content using the "*Heatmap*" function within the "*Complexheatmap*" package version 2.14.0 (Gu et al., 2016; Gu, 2022).

Supervised machine learning techniques, which are prediction-based multivariate analysis techniques used to integrate and analyze the metabolic response, were used, including Partial Least Squares Discriminant Analysis (PLS-DA) and Sparse Partial Least Squares Discriminant Analysis (sPLS-DA), to identify potential metabolic markers, and Receiver Operating Characteristic (ROC) analyses were conducted using the "*mixOmics*" package (version 6.28.0) in R (Rohart et al., 2017). For physiological traits, principal component analysis (PCA) was conducted using the "*factoextra*" package version 1.0.7 (Kassambara and Mundt, 2020) and visualized with the "*ggplot2*" package version 3.4.3 (Wickham, 2016).

For correlation analysis among metabolic, physiological, and gene datasets, we used the Pearson correlation method in the "*psych*" package version 2.3.6 (Revelle, 2023). Significant correlations ($p < 0.05$) with $|r| \geq 0.85$ were filtered and used for network analysis. Correlation-based networks were constructed from the filtered correlation matrices and visualized using *Cytoscape* version 3.10.3 (Shannon et al., 2003) for each variety. A bipartite network was constructed to identify the

possible association of C-metabolites and physiological traits with the sugar metabolism and heat tolerance genes for each variety.

## 3. Results

### 3.1. Characterization of macroclimatic heatwave events and spatial thermal heterogeneity

Macroclimatic temperature profiles exhibited distinct interannual variations across the three study seasons, although all field campaigns were successfully executed during the seasonal thermal peaks of the respective growing periods when maximum ambient air temperatures ($T_a$) were consistently elevated (Fig. 1a). The targeted sampling windows in 2022, 2023, and 2024 took place during naturally occurring heatwave periods characterized by multi-day extreme temperature anomalies. Maximum daily air temperatures during these specific monitoring campaigns frequently exceeded 35 °C, with multiple consecutive days approaching or surpassing 40 °C (Fig. 1a). This environmental backdrop ensured that the downstream physiological and metabolic measurements captured acute vine responses under severe field heat stress rather than baseline summer conditions.

The frequency, monthly distribution, and cumulative duration of these extreme thermal events varied noticeably across years (Fig. 1b). Heatwave episodes, defined as at least 3 consecutive days with a maximum $T_a > 35$ °C, were predominantly concentrated between June and September, with the highest clustering and intensity recorded during midsummer. While all three seasons experienced recurrent heatwave conditions, differences in the timing and monthly distribution of these episodes indicated that the monitored years represented contrasting, independent thermal scenarios rather than identical climatic conditions. This natural macroclimatic variability provided a robust, field-realistic framework for evaluating cultivar-specific adaptive mechanisms and plastic responses to distinct heat-stress profiles.

Concurrently, UAV-derived thermal imagery revealed pronounced spatial heterogeneity in canopy temperature ($T_c$) distribution across the experimental vineyard during active heatwave intervals (Fig. 1c). Distinct and repeatable thermal patterns emerged between individual vines and rows under uniform irrigation scheduling. These localized variations highlighted that heat-stress responses in this desert system were manifested not only temporally across the diurnal timeline but also spatially through contrasting, genotype-specific canopy cooling capacities. This clear baseline thermal differentiation confirmed that macroclimatic conditions successfully triggered cultivar-dependent, variable microclimatic adaptations, establishing a valid foundation for subsequent ground-level physiological and biochemical analyses.

### 3.2. Cultivar-specific diurnal leaf gas exchange and conductance dynamics

Stomatal conductance ($g_s$) exhibited pronounced temporal and cultivar-specific patterns across all evaluated heatwave scenarios (Fig. 2a). Under the acute 2022 thermal anomaly, $g_s$ ranged from 0.1

to 0.6 mol $m^{-2}$ $s^{-1}$, revealing significant diurnal timepoint ($p < 0.05$) and cultivar effects ($p < 0.05$). Values were uniformly higher during the morning and evening intervals relative to midday, illustrating a classic midday stomatal restriction driven by peak diurnal thermal and vapor pressure deficits. Among the evaluated genotypes, Syrah consistently maintained the highest $g_s$, followed by Petit Verdot, whereas Tempranillo exhibited the lowest values. This response ranking was preserved under the 2023 scenario; despite its warmer baseline and less acute daily anomaly, Syrah retained the highest $g_s$, while Tempranillo remained the most conservative across all time points. During the severe 2024 season, Syrah demonstrated robust stomatal resilience, sustaining values up to 0.4 mol $m^{-2}$ $s^{-1}$ while all other cultivars dropped below 0.3 mol $m^{-2}$ $s^{-1}$ ($p < 0.05$). Across years, the absolute magnitude of $g_s$ showed a non-monotonic relationship with seasonal heatwave intensity, whereas Syrah's relative regulatory advantage remained stable across contrasting heat-stress profiles.

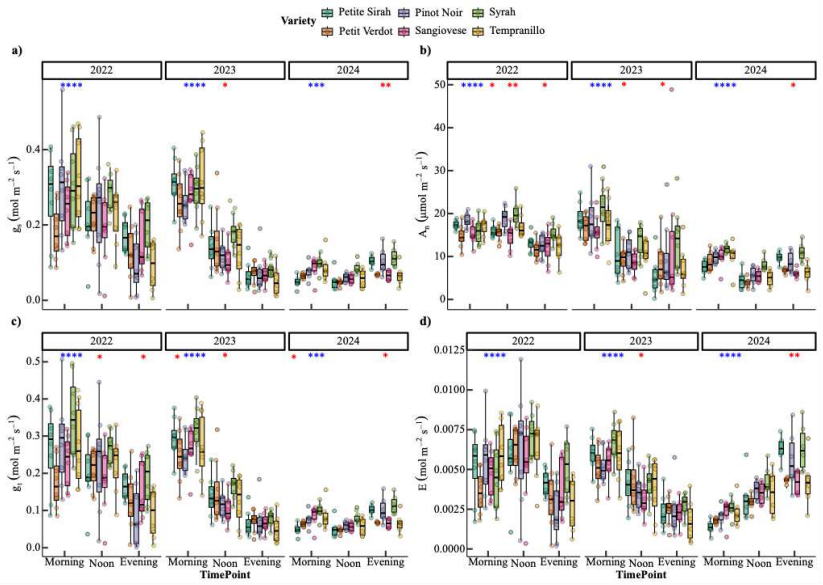



Figure 2: Physiological responses to heatwave events across years. (a) Stomatal conductance ($g_s$), (b) $CO_2$ assimilation rate ($A_n$), (c) total conductance to water vapor ($g_t$), and (d) transpiration rate ($E$). Asterisks indicate significant differences in varieties (red color asterisks) and timepoints (blue color asterisks) ($p < 0.05$).

Net $CO_2$ assimilation rates ($A_n$) tracked distinct cultivar-specific strategies and strong diurnal influences within each heatwave event (Fig. 2b). In the 2022 season, $A_n$ values fluctuated between 5 and 27 µmol $m^{-2}$ $s^{-1}$, with significant ($p < 0.05$) cultivar and timepoint variations. A distinct midday photosynthetic depression occurred across all genotypes. Syrah achieved the highest overall assimilation rates, particularly during the morning and evening recovery windows. Petite Sirah and Petit Verdot also maintained high $A_n$ capacities, whereas Tempranillo displayed consistently lower carbon fixation across all diurnal intervals. Significant main effects and interactions persisted into the 2023 and 2024 campaigns, in which Syrah consistently led in carbon assimilation. Rather than following a strictly linear interannual trend, photosynthetic capacity varied non-monotonically according to event-specific heatwave structures. Tempranillo

consistently defined the lower baseline for carbon assimilation across both seasons, while Syrah anchored the upper threshold during the morning and evening.

Total conductance to water vapor ($g_t$) varied significantly by cultivar and timepoint across all monitored heatwave events (Fig. 2c). During the 2022 campaign, $g_t$ values ranged between 0.3 and 0.5 mol $m^{-2}$ $s^{-1}$ ($p < 0.05$), tracking a typical midday depression followed by a partial evening resurgence. Syrah consistently maximized $g_t$, whereas Sangiovese and Tempranillo exhibited highly restricted water vapor transport, particularly at noon and evening. These explicit temporal trajectories and cultivar hierarchies were structurally maintained through the 2023 and 2024 thermal scenarios, during which Syrah maintained superior overall water vapor conductance. The shifting absolute magnitude of $g_t$ across seasons underscored a non-monotonic interaction between environmental heatwave intensity and total conductance, showing that both anomaly magnitude and baseline seasonal temperatures heavily modulated within-event gas exchange.

Leaf transpiration rates ($E$) demonstrated tight temporal regulation and clear genetic differentiation during each distinct heatwave event (Fig. 2d). Under 2022 conditions, $E$ extended from 0.001 to 0.0125 mol $m^{-2}$ $s^{-1}$, dictated by significant diurnal timepoint effects ($p < 0.05$). Syrah and Pinot Noir showed the highest continuous transpiration rates. Conversely, Tempranillo displayed elevated $E$ exclusively in the morning, shifting rapidly to a conservative water-use strategy during noon and evening intervals. The strict coupling of Syrah's elevated $E$ alongside its high $g_s$ indicates active, open-stomatal evaporative cooling under acute thermal loads. Significant temporal and cultivar differences persisted across the 2023 and 2024 seasons ($p < 0.05$). Syrah consistently logged the highest absolute transpiration rates across all years, illustrating an event-specific interplay between vapor pressure deficit and stomatal aperture rather than a uniform, unidirectional response to rising ambient temperatures.

Total conductance to $CO_2$ ($g_c$) confirmed substantial cultivar and within-day variation across the study (Fig. 3a). In 2022, $g_c$ ranged from 0.05 to 0.35 mol $m^{-2}$ $s^{-1}$, with significant temporal declines observed at noon and evening across all genotypes ($p < 0.05$). Interestingly, Tempranillo exhibited a brief advantage with higher morning $g_c$, but Syrah became dominant at noon and evening, reaching values up to 0.3 mol $m^{-2}$ $s^{-1}$. Petit Verdot and Pinot Noir also maintained high $g_c$ ranges, while Tempranillo and Sangiovese reached the lowest conductance levels as daily thermal stress progressed ($p < 0.05$). During the 2023 and 2024 heatwaves, these significant main effects remained consistent ($p < 0.05$), with Syrah maintaining the highest $g_c$ throughout all diurnal tracking blocks. Across all seasons, $g_c$ followed a non-monotonic distribution governed by the specific thermal regime of each discrete heat event; Tempranillo and Sangiovese regularly marked the lowest noon and evening $g_c$ minimums, while Petit Verdot and Pinot Noir remained elevated.

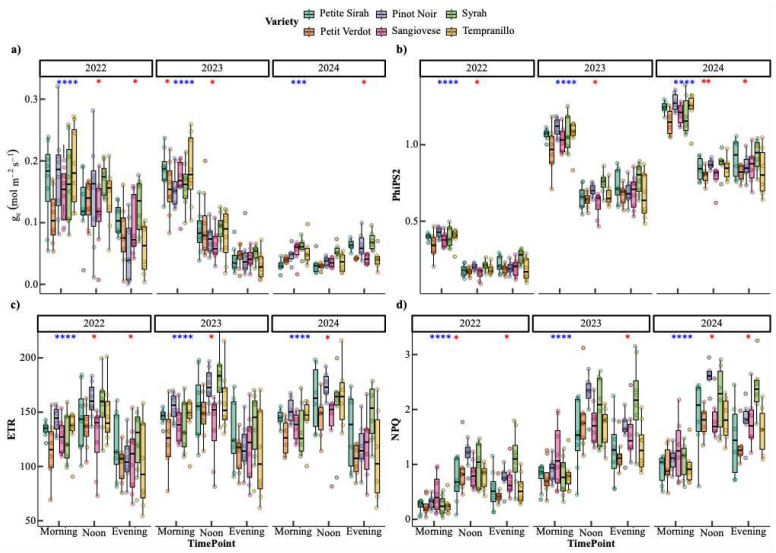



Figure 3: Leaf fluorometric and photosynthetic responses to heatwave events across years. (a) Total conductance to $CO_2$ ($g_c$), (b) effective quantum yield of photosystem II (PhiPS2[$\Phi_{PSII}$]), (c) electron transfer rate (*ETR*), and (d) non-photochemical quenching (NPQ). Asterisks indicate significant differences between varieties (red color asterisks) and timepoints (blue color asterisks) ($p < 0.05$).

### 3.3. Leaf chlorophyll fluorescence and photochemical efficiency traits

The effective quantum yield of photosystem II ($\Phi_{PSII}$) demonstrated pronounced temporal dynamics and cultivar-specific profiles during each evaluated heatwave campaign (Fig. 3b). In the 2022 season, $\Phi_{PSII}$ ranged from 0.2 to 0.5, tracking significant diurnal timepoint effects ($p < 0.05$). The lowest values occurred uniformly at midday across all genotypes, indicating transient midday photoinhibition, which was followed by partial photoprotective recovery during the evening interval. Among the evaluated cultivars, Syrah exhibited the highest quantum yields, followed by Pinot Noir and Petite Sirah. Conversely, Sangiovese and Tempranillo displayed the lowest $\Phi_{PSII}$ baseline efficiencies, confirming significant genetic variance in photochemical resilience under acute heat stress ($p < 0.05$). During the 2023 and 2024 heatwaves, these intra-event temporal and cultivar hierarchies were maintained: Syrah consistently maintained comparatively higher $\Phi_{PSII}$ values, whereas Sangiovese and Tempranillo remained the most severely impacted across both seasons.

The chloroplastic electron transport rate (*ETR*) displayed distinct cultivar and diurnal responses within each heatwave scenario (Fig. 3c). During the 2022 campaign, *ETR* values ranged between 50 and 200 µmol $m^{-2}$ $s^{-1}$, with significant temporal shifts ($p < 0.05$) showcasing sharp midday elevations driven by high incident solar irradiance. Syrah, followed closely by Tempranillo and Pinot Noir, achieved the highest overall light-driven electronic flux, reaching peak values of 180–200 µmol $m^{-2}$ $s^{-1}$ at noon. In contrast, Petit Verdot and Sangiovese exhibited constrained transport capacities, highlighting significant cultivar-specific differences under peak thermal stress ($p < 0.05$). Under the 2023 and 2024 microclimatic conditions, this structural intra-event cultivar

framework was preserved, with significant genetic variations in midday ETR ($p < 0.05$) persisting across both independent heatwave periods.

Non-photochemical quenching (NPQ**)** tracking revealed distinct photoprotective dissipation strategies among the grapevine cultivars within each discrete heatwave event (Fig. 3d). During the 2022 campaign, NPQ values varied widely from 0.1 to 2.0, with significant timepoint effects ($p < 0.05$) indicating a strong induction of thermal energy dissipation during both the midday and evening intervals. Tempranillo consistently maintained the highest NPQ values, followed by Pinot Noir and Sangiovese, confirming a heavy reliance on non-radiative energy dissipation mechanisms to prevent irreversible photosystem damage. Conversely, Syrah exhibited moderate NPQ induction alongside its superior net photosynthetic performance, while Petite Sirah displayed the lowest overall quenching levels ($p < 0.05$). Throughout the 2023 and 2024 heat-stress periods, Syrah maintained a highly efficient balance of NPQ and elevated carbon assimilation, while Tempranillo, Pinot Noir, and Sangiovese repeatedly displayed high quenching coefficients, reflecting a high requirement for photoprotective thermal dissipation under stress.

## 3.4. UAV-Based Thermal Phenotyping and Multi-Scale Temperature Dynamics

### 3.4.1. Leaf-Scale Thermal Load Analysis

In situ leaf temperatures ($T_{leaf}$) recorded via the gas exchange chamber mirrored ambient conditions but tracked substantial diurnal and cultivar-specific shifts across all heatwave events (Fig. 4a; Fig. S1). During the 2022 campaign, $T_{leaf}$ climbed from an ambient coupled morning baseline of ~25 °C to an acute peak of ~39 °C at noon, demonstrating significant diurnal timepoint influences ($p < 0.05$). At peak midday stress, Syrah exhibited the highest absolute $T_{leaf}$, followed closely by Tempranillo and Sangiovese. Conversely, Petite Sirah and Petit Verdot maintained cooler local leaf thresholds, averaging ~36 °C, confirming significant cultivar divergence at the individual lamina scale ($p < 0.05$). Similar multivariable hierarchies were observed during the 2023 season. During the severe 2024 heatwave, absolute thermal loads intensified further, pushing peak $T_{leaf}$ values to 42 °C, with Tempranillo, Sangiovese, and Syrah consistently registering the highest boundary-layer temperatures.

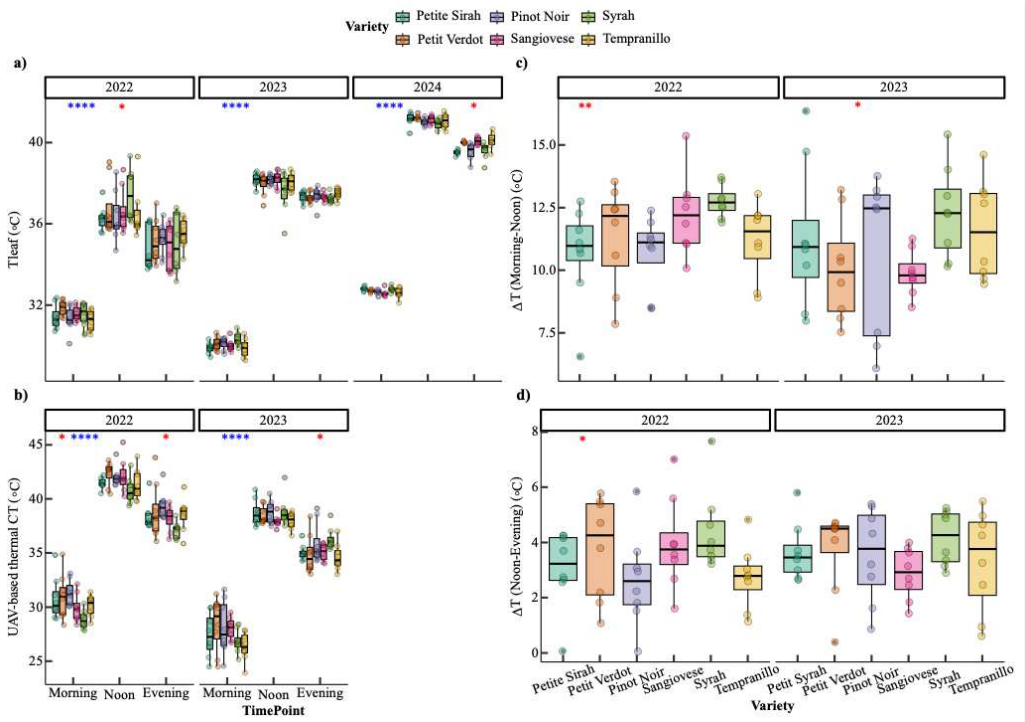



Figure 4: Leaf temperature (ground measurement) and UAV-captured canopy temperature (CT). (a) leaf temperature measurements measured using the LI-6800 portable photosynthesis system, (b) thermal image-derived canopy temperature profiles for each grapevine variety, delta temperature (ΔT) refers to the difference between two daily temperatures; (c) between Morning to Noon and (d) between Noon to Evening. Asterisks indicate significant differences between varieties (red) and timepoints (blue) ($p < 0.05$).

### 3.4.2. UAV canopy-scale thermal tracking and cross-scale integration

UAV-derived absolute canopy temperatures ($T_c$) revealed a contrasting structural pattern compared to individual leaf-scale sensors (Fig. 4b). Despite exhibiting elevated leaf-scale chamber temperatures, Syrah consistently maintained the lowest macro-canopy thermal profile across the diurnal monitoring windows. Its whole-canopy framework remained 2–5 °C cooler than the warmest genotypes in the vineyard. This divergence indicates that single-leaf thermal boundaries did not dictate macro-canopy heat accumulation. Instead, it reflects a superior whole-canopy latent heat flux and evaporative cooling capacity fueled by Syrah's sustained stomatal conductance and $E$ (Fig. 2a, d). Conversely, Petit Verdot, Tempranillo, Pinot Noir, and Sangiovese, which displayed moderate to low localized $T_{leaf}$ in the chamber, registered the highest spatial canopy temperatures, while Petite Sirah maintained an intermediate thermal position ($p < 0.05$). Across the 2022 tracking dates, $T_c$ varied dynamically between 25 and 42 °C, driven by expected diurnal radiation loads ($p < 0.05$), and these cultivar rankings remained stable into the 2023 monitoring campaign.

Following radiometric calibration and template coregistration, ground-validated leaf metrics and UAV-derived spatial datasets exhibited a strong, highly significant correlation ($R^2 = 0.80$) (Fig. S1f). Non-parametric analysis confirmed that within-day thermal trajectories diverged sharply

across temporal windows; the morning-to-noon canopy temperature shift averaged 1.91 °C (Bonferroni-corrected $p < 0.0001$), while the noon-to-evening cooling trajectory averaged 1.32 °C (Bonferroni-corrected $p < 0.00015$) (Fig. S2e, f). This statistical alignment validates the use of high-frequency aerial remote sensing to accurately track diurnal microclimatic adjustments in real time under hyperarid conditions.

Afternoon canopy cooling trajectories quantified as the change in canopy-to-air temperature differentials from noon to evening ($\Delta T_{noon–evening}$) ranged from 1 to 8 °C across the evaluated germplasm (Fig. 4d). Under the 2022 thermal anomaly, Tempranillo, Pinot Noir, and Sangiovese exhibited the most pronounced afternoon cooling dynamics. This steep decline was directly coupled with their high midday canopy thermal loading. Conversely, Syrah demonstrated more moderate afternoon cooling (4–6 °C), highlighting a well-buffered, stable macro-canopy thermal regime throughout the diurnal cycle ($p < 0.05$). Similar relative thermal trajectories were preserved during the 2023 season.

### 3.4.3. Unsupervised structural clustering of thermal phenotypes

To classify these empirical surface-temperature variations without taxonomic bias, an unsupervised partitioning model was deployed on the UAV-derived thermal datasets. The variance ratio criterion identified two distinct, statistically optimal phenotypic groups across the multi-year campaigns (Table S.1; Fig. S2a-d). Cluster 1 was characterized by an active thermal response phenotype, displaying steep morning-to-noon heating slopes coupled with strong, high-amplitude afternoon cooling trajectories. Cluster 2 manifested a more thermally stable phenotype, defined by moderate morning-to-noon heating rates and attenuated diurnal fluctuations. The distribution of individual vines across these clusters revealed that the canopy thermal phenotype was not rigidly fixed by genetics alone (Table S.2). Notable exceptions to this plastic behavior emerged during specific seasons: 100% of the Syrah replicates were assigned to Cluster 1 during the 2022 campaign, whereas 100% of the Sangiovese replicates clustered into Cluster 2 during the 2023 heatwave event.

To isolate the precise features driving this spatial grouping, a principal component analysis (PCA) was integrated with a fuzzy *c*-means (FCM) clustering algorithm based exclusively on the aerial canopy temperature metrics (Fig. 4e). The first two principal components captured 63.2% of the total cumulative variance, with PC1 accounting for 35.8% and PC2 for 27.4% of the data structure. The continuous membership vectors generated by the FCM model shifted dynamically across both cultivars and independent campaign years. This fluid partitioning mathematically confirms that grapevine canopy thermal phenotypes in hyperarid environments are governed by a complex, event-specific interaction between genotype and localized microclimatic stress intensity rather than strict, unyielding varietal characteristics.

Principal component analysis of the complete physiological dataset confirmed strong temporal structuring across all heatwave scenarios, capturing high cumulative explained variances across

all years (Fig. 5). Spatial coordinate distributions revealed that morning data points were widely dispersed across the multivariate space, driven primarily by strong loading vectors from $g_s$, $g_c$, and $\Phi_{PSII}$. As the daily thermal stress progressed, noon and evening coordinate clusters converged tightly during the moderate 2023 season, whereas they maintained wide separation during the severe 2024 campaign (Fig. 5). Interannual comparison showed a clear shift in primary discriminating variables: the main physiological drivers transitioned from $g_s$, $g_c$, and $\Phi_{PSII}$ under the acute 2022 anomaly toward $\Phi_{PSII}$ and $E$ during the high-intensity 2024 heatwave event.

This transition indicates that photosystem efficiency and continuous whole-canopy latent heat dissipation become the ultimate physiological differentiators of grapevine resilience under extreme thermal stress.

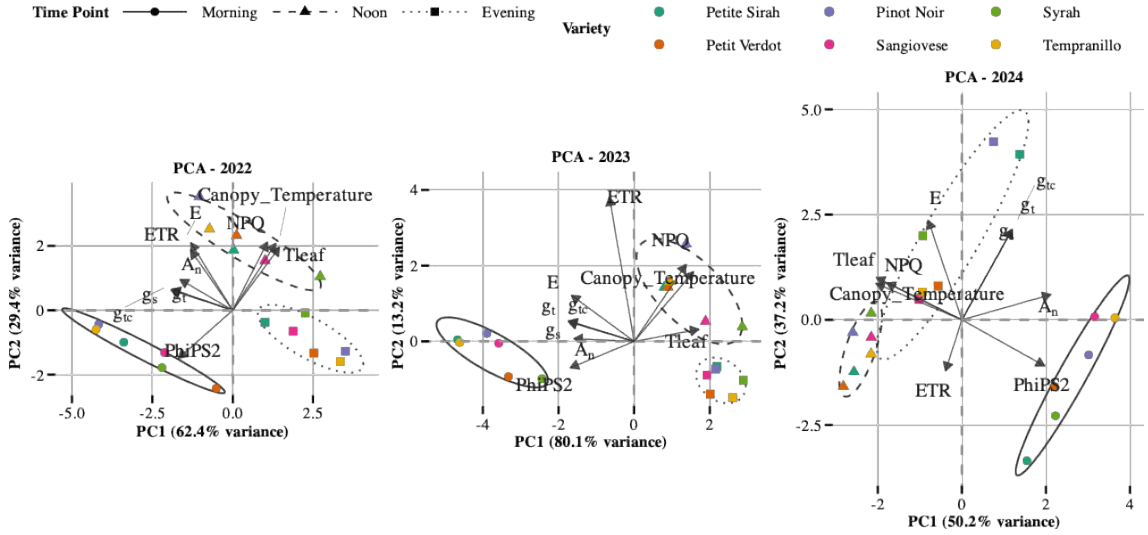



Figure 5: Diurnal patterns of heatwave response vary among grape varieties and across years. Principal Component Analysis (PCA) of physiological traits across three years (2022-2024) reveals distinct timepoint-driven dispersion patterns (morning, noon, evening), with loading vectors indicating the relative contribution of each measured parameter to the observed variance. Ellipses represent 95% confidence intervals grouped by sampling timepoint.

### 3.5. Primary metabolite profiling and interannual flux dynamics

Comprehensive primary metabolic profiling over the three-year study period (2022–2024) uncovered highly coordinated temporal and cultivar-specific shifts in leaf metabolite profiles (Fig. 6a). Amino acids showed extreme flux sensitivity across all experimental settings. The coefficient of variation (CV) exceeded 60–80% for nitrogen compounds, including serine, alanine, aspartate, valine, γ-aminobutyric acid (GABA), and glutamine. Organic acids maintained robust homeostasis with low baseline variation (CV 20–40%), signaling a stable metabolic flux through the core tricarboxylic acid (TCA) cycle. Phosphorylated intermediates such as glucose-1-phosphate and fructose-6-phosphate displayed moderate variability (CV 40–60%) and accumulated during the evening recovery windows.

Cultivars diverged sharply in their metabolic plasticity under acute thermal conditions. Pinot Noir and Tempranillo exhibited localized variations in the accumulation of structural transport sugars (sucrose, glucose, and fructose), polyols (mannitol and *myo*-inositol), and hexose phosphates during the noon and evening phases. Conversely, Petite Sirah and Syrah initiated the most active protective metabolism, characterized by high concentrations of low-molecular-weight nitrogenous compounds (glutamine, proline, and GABA) and elevated polyols. Syrah and Petit Verdot were distinguished by superior preservation of organic acids, particularly malate, citrate, and shikimate, at noon and in the evening. Sangiovese showed an intermediate metabolic response, with an isolated upregulation of the polyols. Petit Verdot showed the least dynamic, chemically conserved primary metabolic footprint under acute thermal stress.

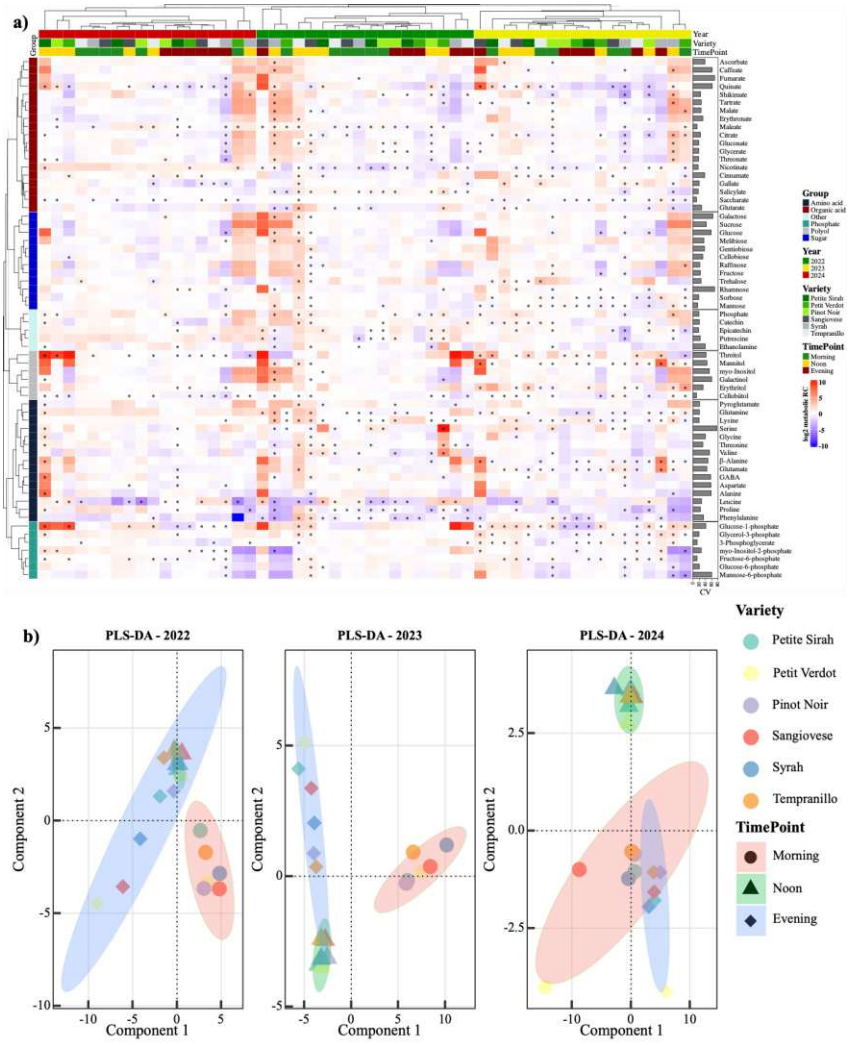



Figure 6: Central metabolic profiling under heatwave stress. (a) Metabolic responses of different red grapevine varieties under heatwave conditions. The heatmap (center) displays the $\log_2$ relative metabolite content (normalized to the internal standard) using a color gradient. The bar graph (right) represents the coefficient of variation, calculated as the standard deviation divided by the mean across the population (n = 6-8). b)Year-specific two-dimensional PLS-DA score plots showing temporal metabolic differentiation. Concentration ellipses represent 95% confidence

intervals encompassing data points from all seasons and biological replicates. Individual data points correspond to an average across replicates (6-8) of six varieties per season per timepoint.

Diurnal tracking revealed tightly orchestrated metabolic cycles across all cultivars. Morning samples were defined by baseline levels of organic acids, except for isolated accumulations of malate, citrate, and tartrate in Petit Verdot. At midday, a uniform metabolic shift triggered a major accumulation of amino acid osmolytes (GABA, proline, and glutamate) and specific organic acids across the vineyard, which subsided during the evening. The evening recovery phase was characterized by a distinct accumulation of structural carbohydrates and polyols, with glucose, fructose, and sucrose reaching peak relative abundances in Sangiovese and Petit Verdot.

On an annual scale, the three-year dataset revealed distinct climatic fingerprints. The 2023 season triggered a systemic accumulation of compatible solutes and low-molecular-weight osmolytes across all cultivars. While structural sugar processing remained uniform across all seasons, the amino acid profiles showed highly variable interannual patterns, with the content increased in the primary stress-responsive pathways (Fig. 6a).

### 3.6. Multivariate chemometric models and temporal biomarker identification

Partial least squares discriminant analysis (PLS-DA) established distinct, year-specific metabolic trajectories across the three-year timeline (Fig. 6b, Fig. S3a-c). This separation was validated by the corresponding receiver operating characteristic (ROC) curves (Fig. S5a-c). The two-dimensional score plots resolved the temporal variance along the first two latent variables. In 2022, sample coordinates clustered tightly with minimal spatial separation between diurnal phases, confirming a rigid, unshifted metabolite profile. The 2023 dataset resolved clear discrimination along Latent Variable 1, with morning and evening data points forming separate clusters and noon samples showing an intermediate distribution. The 2024 campaign generated the most pronounced temporal separation, with clear, non-overlapping separation of all three diurnal timepoints across both principal coordinates (Fig. 6b).

PLS-DA loading analyses highlighted the individual metabolic drivers responsible for this diurnal discrimination across the growing seasons (Fig. S3a-c). The morning profiles were differentiated by specific free amino acids (lysine, pyroglutamate, and phenylalanine) and central carbon intermediates (citrate, malate, fumarate, sucrose, glucose, inorganic phosphate, shikimate, maleate, gluconate, and fructose-6-phosphate). The midday profiles showed the greatest separation, driven by free carbohydrates, including trehalose, glucose, sucrose, sorbose, and mannose. The evening recovery samples showed minimal separation.

Cross-validation routines confirmed the statistical robustness of the predictive chemometric models (Fig. S4). Both the 2022 and 2024 models achieved high classification accuracies with 2 to 3 latent variables, maintaining balanced classification error rates well below 0.30. The 2023 model demonstrated superior predictive power, achieving optimal sample classification with just 2 components while maintaining low error rates (~0.05) across all distance metrics. The stable

cross-validation curves and rapid error-rate stabilization confirm reliable, reproducible temporal metabolic discrimination. The maximum distance metric outperformed both the centroid and Mahalanobis distance approaches (Fig. S4d).

To isolate a minimized set of diagnostic markers, feature selection was performed using a sparse PLS-DA (sPLS-DA) algorithm via the mixOmics package. This pipeline identified 10 key metabolites per campaign, along with a global feature set, as putative metabolic biomarkers for temporal stress classification (Table 1). This optimized subset achieved a balanced error rate below 0.15 on the first predictive component (Fig. S4d). The feature selection curve showed a rapid drop in classification error, which plateaued at exactly 10 features, mathematically confirming that a compact, focused set of core primary metabolites captures the temporal metabolic variance across grapevine cultivars and distinct heatwave intensities.

Table 1: Putative metabolic biomarkers with diurnal temporal responses for a heatwave event. Features were identified using an sPLS-DA model based on mixOmics. Global analysis merged all samples, while stratified analyses separated data by timepoint (morning, noon, evening) and year (2022, 2023, 2024). Selected metabolites persist across time points, with peak variance from morning to evening. Bolded text highlights features selected more than once across years.

| 2022 features | 2023 features | 2024 features | Global features |
|---|---|---|---|
| **Pyroglutamate** | Galactinol | **Leucine** | Nicotinate |
| **Leucine** | Sucrose | Raffinose | Epicatechin |
| Glycerate | myo-Inositol | **Maleate** | Proline |
| **Maleate** | **Pyroglutamate** | Malate | myo-Inositol-2-phosphate |
| **Fructose** | Caffeate | Glycine | Putrescine |
| Shikimate | Erythronate | **Fructose** | Threitol |
| Phosphate | Malate | Mannose | Glucose-1-phosphate |
| Gluconate | Fumarate | Sorbose | Lysine |
| Phosphoglycerate | Galactose | **Pyroglutamate** | Glutamine |
| Alanine | **Fructose** | Threonate | GABA |

3.7. Transcriptional profiling of heat tolerance and sugar metabolism

Quantitative real-time PCR (qRT-PCR) analysis revealed distinct, coordinated transcript accumulation profiles for genes governing heat tolerance, transmembrane sugar transport, and hexose biosynthesis across the evaluated grapevine cultivars (Fig. 7). A subset of candidate genes, specifically *HT3*, *HT5*, and *PGTR1*, exhibited broadly uniform expression levels with minimal genetic or diurnal variance under the monitored heatwave scenarios. In contrast, several hexose transporter and carbohydrate biosynthesis genes demonstrated pronounced, cultivar-specific temporal induction patterns: *HT1*, *HT2*, and *HT6* displayed sharp upregulation at midday (12:00) in Petit Verdot and Tempranillo, whereas their transcript abundance peaked during the morning (07:00) in Pinot Noir. *HT4* and *SUC2* exhibited robust, localized expression at midday in Petite

Sirah, with *SUC2* also displaying significant midday induction in Sangiovese. *SUS3* transcript induction was maximal at midday in Syrah. *SWEET10* and *ERD6L* showed strong, early-morning upregulation in Petit Verdot and Petite Sirah; *ERD6L* additionally maintained a distinct secondary peak at noon in Tempranillo, a pattern consistent with rapid, early-stage osmotic stress signaling.

Collectively, the midday interval emerged as the primary transcriptional induction node across most evaluated genes and cultivars. This synchronized upregulation directly corroborates the noon-specific primary metabolic profiles resolved by the multivariate PLS-DA models, providing strong evidence for a rigidly coordinated within-day stress response that links core thermotolerance machinery with active carbohydrate translocation networks.

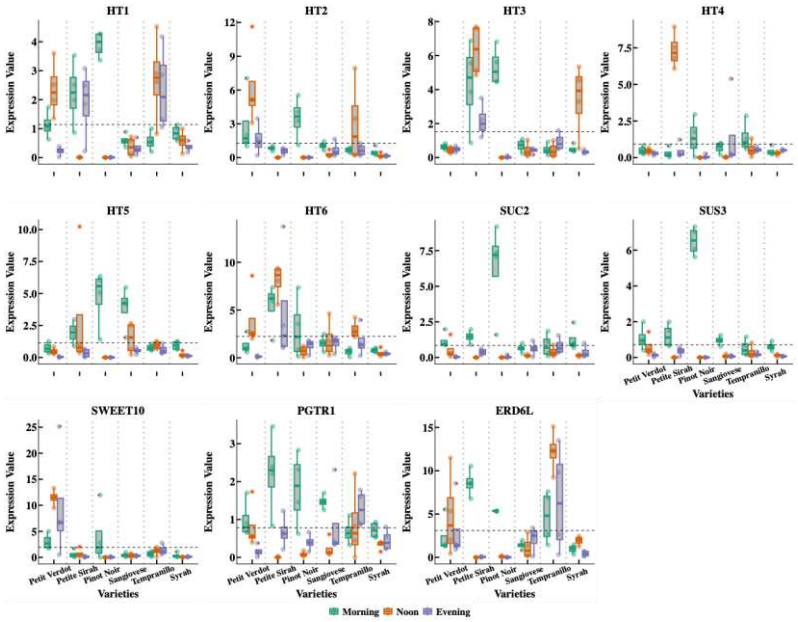



Figure 7: Expression level of heat-shocking, sugar-synthesis, and sugar-transporter genes across time points in the day during a heatwave event in different red grapevine varieties. The dashed horizontal line indicates the median of the expression level across varieties.

3.8. Topological analysis of integrative correlation-based networks

To contextualize the molecular and physical interactions driving these stress responses, a multi-scale correlation network analysis was performed by integrating primary metabolite profiles, transcript abundance datasets, leaf gas exchange metrics, and UAV-derived thermal traits across all six cultivars (Fig. 8a-f). The systemic network topology successfully corroborated and interconnected the empirical trends observed within the individual datasets.

Network complexity metrics varied noticeably by cultivar, with total node counts ranging from 71 (Pinot Noir) to 88 (Petit Verdot, Sangiovese, and Tempranillo). The networks maintained a uniform diameter of 5 across most genotypes, except for Petite Sirah, which exhibited a diameter of 6, while network clustering coefficients ranged from 0.603 to 0.778 (Fig. 9c). Syrah and Sangiovese manifested highly specialized, stable network topologies, with Syrah exhibiting a high

clustering coefficient (0.773) and moderate network density (0.222) spread across three discrete connected components. Pinot Noir exhibited the highest absolute network density (0.328) and clustering coefficient (0.778) yet was restricted to a fragmented structure spanning five independent components, signaling compartmentalized rather than systemic physiological coordination (Fig. S6h, k). Tempranillo maintained a single, fully connected macro-component but displayed the longest characteristic path length (2.359) and the highest overall network heterogeneity (0.884). This diffuse topology indicates loose coordination and less efficient physiological integration across the measured phenotypic traits (Fig. S6c, i).

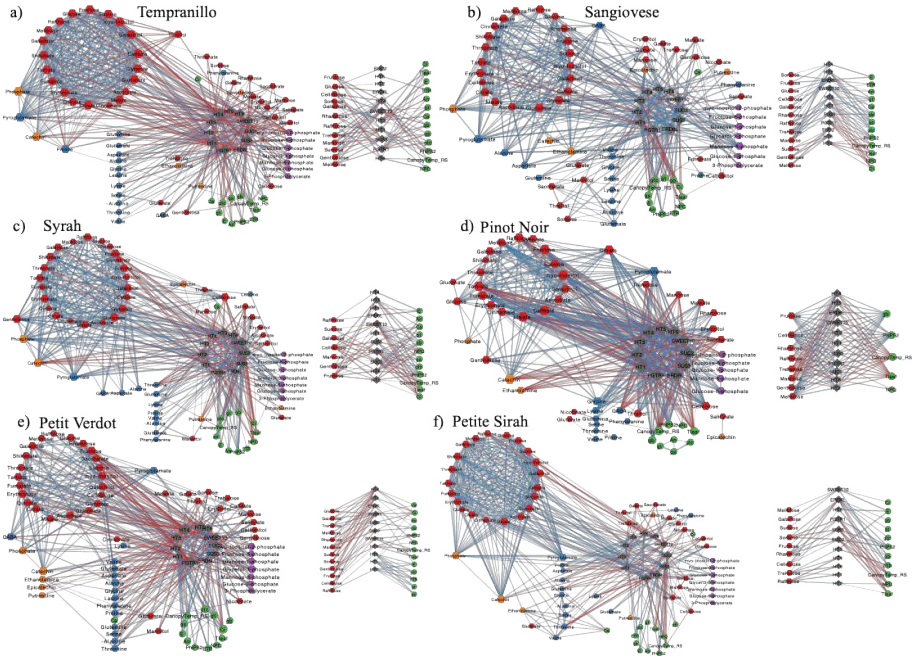



Figure 8: Correlation-based metabolic networks of six grape varieties under heat stress conditions. Networks show relationships between metabolites, thermal measurements, sugar metabolism genes, and physiological traits in leaves of (a) Tempranillo, (b) Sangiovese, (c) Syrah, (d) Pinot Noir, (e) Petit Verdot, and (f) Petite Sirah. A complementary bipartite network illustrates direct and indirect regulatory relationships between sugar metabolism genes, sugar metabolites, and physiological responses. Network construction: Nodes represent different molecular and physiological components, color-coded by category. Edges represent significant Pearson correlations ($p < 0.05$, $|r| > 0.85$) between all pairwise combinations of variables. Edge colors indicate correlation direction (red = positive, blue = negative), while edge width reflects correlation strength. Node size corresponds to degree centrality (number of connections).

Nodal centrality metrics identified core heat tolerance transcripts (*HT1–HT6*) and sugar metabolism genes (*SWEET10*, *SUC2*, and *SUS3*) as highly connected, system-wide hubs with degree values exceeding 30 connections across all cultivars. Among these, *HT4* consistently emerged as the node with the highest composite importance, as measured by Variable Importance in Projection (VIP) scores (Fig. S7a, g; Fig. 8a, b). Furthermore, the vacuolar and plastidic sugar transport genes *ERD6L* and *PGTR1* generated the highest absolute betweenness centrality (>0.6) and stress values (>40,000) (Fig. 9b, h). This positions them as primary cross-module informational bridges linking carbohydrate processing, amino acid biosynthesis, secondary

phenolic pathways, and downstream cellular stress responses, which aligns with their diurnal expression trajectories.

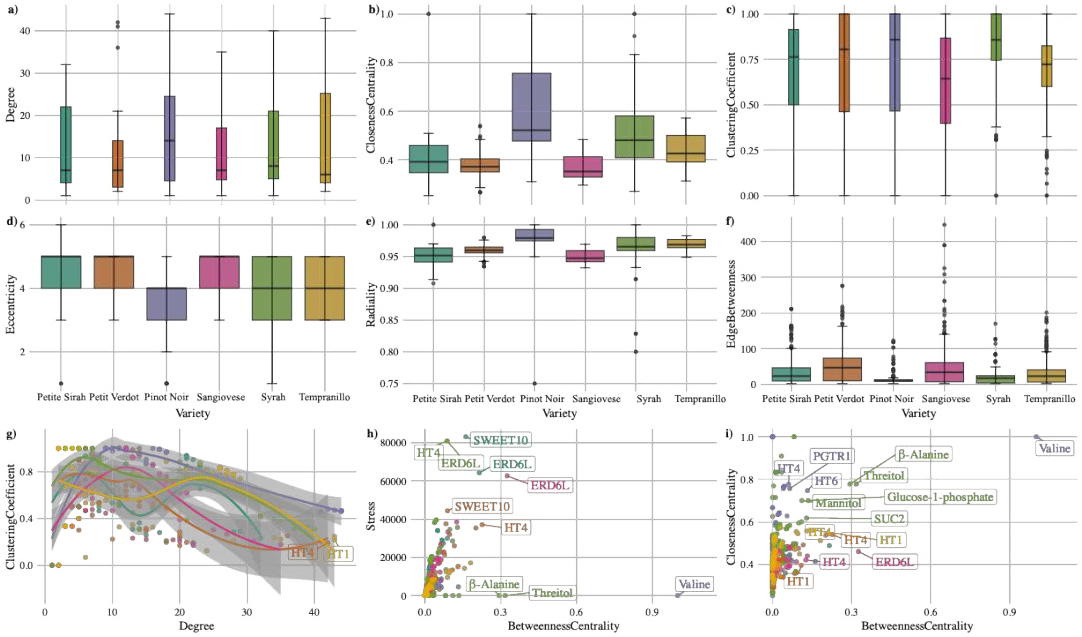



Figure 9: Topological analysis of correlation-based metabolic networks across six grape varieties. Distribution of key network properties: (a) node degree, (b) closeness centrality, (c) clustering coefficient, (d) eccentricity, (e) radiality, and (f) edge betweenness centrality. Pairwise relationships between network measures: (g) clustering coefficient versus node degree, (h) network stress versus betweenness centrality, and (i) closeness centrality versus betweenness centrality. Each variety is distinguished by color coding. These metrics collectively characterize the structural organization and connectivity patterns of variety-specific metabolic networks under heat stress conditions.

At the chemical level, central carbon metabolites (glucose, fructose, and sucrose), along with the primary stress osmolytes proline and GABA, consistently yielded elevated VIP scores, providing direct, independent validation of the noon metabolic markers identified by the PLS-DA model. Taken together, these network topologies confirm that the observed physiological, transcriptional, and metabolic shifts do not function as isolated events; instead, they operate within a coordinated, cultivar-specific stress architecture. This multi-scale alignment demonstrates that the microclimatic resilience classifications derived from automated UAV thermal phenotyping are directly supported by the intrinsic, structural properties of each grapevine cultivar's integrative biological network.

## 4. Discussion

### 4.1. The cross-scale thermal paradox and canopy evaporative thermoregulation

This study establishes a comprehensive field-based assessment of how commercial grapevine varieties respond to natural heatwave events under extreme desert conditions. By integrating multi-scale observations, our findings demonstrate that varietal heat tolerance is manifested as a coordinated, whole-plant microclimatic strategy rather than a series of isolated trait variations.

A primary finding of this framework is the cross-scale thermal paradox observed in the cultivar Syrah. At peak midday stress, Syrah recorded the highest localized leaf-scale temperatures within the gas exchange chamber, yet concurrently maintained the lowest UAV-derived whole-canopy absolute thermal profile, resting 2–5 °C cooler than sensitive cultivars like Tempranillo. This cross-scale disconnect is explained by boundary-layer dynamics and continuous latent heat dissipation under severe VPD. Inside a clamped gas-exchange chamber, forced ventilation alters the natural boundary-layer resistance of an individual leaf lamina, exposing its localized boundary layer to extreme ambient temperatures. However, at the macro-canopy scale under open field conditions, Syrah's uninhibited stomatal conductance and high *E* drive a continuous evaporative cooling. This extensive transpirational flux effectively buffers the broader vine crown microclimate against extreme ambient temperatures, consistent with evaporative thermoregulation as a primary heat-tolerance mechanism (Rogiers et al., 2012; Sadras et al., 2012; Faralli et al., 2022).

The high correlation ($R^2 = 0.80$) obtained between the ground-validated leaf metrics and the UAV-derived spatial datasets confirms that thermal remote sensing captures biologically meaningful, functional stress phenotypes under field conditions (Fig.S1f). This cross-scale alignment validates the deployment of automated aerial imagery to accurately track diurnal microclimatic adjustments in real time in hyperarid viticultural systems (Burchard-Levine et al., 2024).

4.2. Functional trade-offs in stomatal strategies and photochemical efficiency

The pronounced cultivar-specific differences resolved across the three independent heatwave campaigns reveal contrasting, divergent adaptive strategies among the grapevine germplasm. Syrah's capacity to maintain elevated stomatal conductance (up to 0.6 mol $m^{-2}$ $s^{-1}$) and high net $CO_2$ assimilation rates (up to 27 µmol $m^{-2}$ $s^{-1}$) under peak thermal load points to a strategy of stomatal deregulation (Greer, 2024). Keeping the stomata open during acute heat is its primary microclimatic buffering mechanism. Critically, however, this exact physiological trait represents a well-documented hydraulic liability under prolonged soil water deficits. In drought scenarios, Syrah's delayed stomatal closure accelerates hydraulic tension, increasing its vulnerability to severe xylem cavitation and acoustic emissions (Hochberg et al., 2013; Gambetta et al., 2020). This functional trade-off, in which a single stomatal behavior confers a clear microclimatic advantage during atmospheric heatwaves but triggers structural vulnerability under soil drought, underscores the acute context-dependence of viticultural stress tolerance. It highlights the need for scenario-specific phenotyping when selecting plant materials for changing climates (Dou et al., 2024; Wilson et al., 2024). Conversely, Tempranillo exhibited a highly conservative stomatal strategy, characterized by low $g_s$ and constrained assimilation rates. While this isohydric-like behavior protects the vascular pathway from cavitation during drought, it incurs a severe thermal cost during independent heatwaves, causing a sharp midday functional decline and elevated canopy heat accumulation due to suppressed latent heat loss.

Chlorophyll fluorescence tracking provides clear biophysical insights into the downstream consequences of these divergent stomatal strategies. Syrah maintained elevated $g_c$ (0.35 mol $m^{-2}$ $s^{-1}$) and high ETR (180-200 μmol $m^{-2}$ $s^{-1}$) at noon, confirming that its open-stomatal cooling successfully protected $\Phi_{PSII}$ and maintained active linear electron flux despite peak environmental thermal loads (Bernardo et al., 2018; Neri et al., 2024).

In contrast, Tempranillo exhibited severe biophysical decoupling, with relatively high ETR values and highly restricted $g_s$. This mismatch indicates that Tempranillo continued to harvest light energy and drive light-dependent thylakoid reactions, but lacked a sufficient internal $CO_2$ pool to feed the Calvin-Benson cycle. Such a decoupling implies a localized failure to safely process or channel excitation energy through downstream carbon-fixing metabolism. Consequently, the elevated NPQ values observed in Tempranillo, Pinot Noir, and Sangiovese reflect a critical, compensatory photoprotective upregulation (Lauterberg et al., 2024; Zuo, 2025). These cultivars must rely heavily on non-radiative thermal energy dissipation to prevent irreversible singlet oxygen generation and photooxidative destruction of the core reaction centers. Syrah's capacity to maintain moderate NPQ alongside superior net photosynthetic assimilation rates indicates a balanced photoprotective state that avoids excessive thermal energy waste. Furthermore, Tempranillo's temporal pattern, characterized by higher morning $g_c$ values followed by a sharp midday and evening depression, reflects an avoidance strategy. It shifts carbon fixation to the cooler early-morning hours to escape peak diurnal thermal stress, rather than maintaining active metabolic regulation across the full diurnal cycle (Qiu et al., 2025).

### 4.3. Spatial heterogeneity and diurnal recovery dynamics via aerial imagery

High-frequency UAV-based thermal analysis revealed that all evaluated grapevine cultivars followed a shared, overarching diurnal trajectory: morning-to-noon canopy heating, followed by partial recovery from noon to evening. The presence of this consistent afternoon cooling curve across all genotypes demonstrates that the fundamental physiological capacity for thermal recovery was preserved irrespective of baseline sensitivity. The key functional distinction among the cultivars was therefore not the presence or absence of this diurnal path, but rather the absolute magnitude and interannual consistency of their canopy temperature modulation during peak stress periods (Gambetta et al., 2020; Marchin et al., 2022).

Syrah's ability to consistently maintain a cooler, thermally buffered macro-canopy architecture represents an open-canopy, anisohydric thermoregulatory strategy (Tombesi et al., 2015). This behavior effectively distinguishes it from cultivars that exhibit greater plant-to-plant variability or excessive midday heat accumulation. Furthermore, our multi-year comparison demonstrates that macroclimatic differences between the monitoring campaigns were governed by event-specific intensity and cumulative heatwave duration rather than arbitrary year identity. For example, the 2022 heatwave generated much sharper diurnal thermal contrasts than the 2023 season, which had

a higher baseline. This interaction highlights the need to evaluate canopy-to-air temperature differentials within the specific environmental context of each weather anomaly.

Finally, the high within-cultivar spatial heterogeneity resolved by the high-resolution UAV thermal maps underscores that microenvironmental factors, including row orientation, local incident radiation loads, row-edge effects, and localized micro-VPD gradients, interact continuously with the plant genotype to shape the final canopy thermal expression. Together, these results validate UAV-based radiometric thermal imaging as an accurate, high-throughput phenotyping tool. It successfully resolves genotype-level thermoregulatory differences under field heatwave conditions, providing actionable criteria for cultivar selection, vineyard design, and climate adaptation strategies in arid and semi-arid viticultural regions (Venios et al., 2020).

### 4.4. Differential metabolic readjustment defines varietal thermotolerance mechanisms

Significant varietal and temporal metabolic shifts highlight inherent genetic diversity in stress tolerance mechanisms within *Vitis vinifera* under heatwave stress (Hewitt et al., 2023). The elevated midday accumulation of amino acids, particularly GABA, proline, and glutamine, in Petite Sirah and Syrah represents an active stress-buffering strategy. These compatible solutes act as osmoprotectants that maintain cellular and protein membrane integrity, provide alternative nitrogen sources during compromised primary assimilation (Botton et al., 2022), and preserve metabolic homeostasis under peak thermal loads (Ghosh et al., 2021). Conversely, the evening accumulation of soluble transport sugars (glucose, fructose, and sucrose) and polyols (mannitol and *myo*-inositol), especially in Sangiovese and Petit Verdot, reflects a post-stress shift in carbon allocation toward osmotic adjustment and cellular repair (Werner et al., 2020).

The ten key diagnostic biomarkers identified via sPLS-DA span four physiologically coherent functional groups (Table 1; Fig. S4d). Osmoprotective raffinose family oligosaccharides (RFO), specifically galactinol and *myo*-inositol (Salvi et al., 2018), and sucrose in 2023, along with raffinose in 2024, reflect heat shock factor-regulated osmoprotection adjusted to event-specific intensities (Nayak et al., 2023; Tian et al., 2025). Proline, GABA, and putrescine emerged as interannual features that underpin a conserved core osmotic adjustment and ROS scavenging network. The recurrent appearance of pyroglutamate further signals sustained proline-glutamate cycling across repeated heatwaves. Season-specific organic acids, glycerate and phosphoglycerate in 2022, fumarate in 2023, and malate and maleate spanning 2022–2024, suggest tricarboxylic acid (TCA) cycle and photorespiratory adjustments tracking individual weather anomalies. Finally, the selection of nicotinate and epicatechin indicates a sustained requirement for nicotinamide adenine dinucleotide salvage metabolism and phenolic antioxidant protection across all heat-stress scenarios (Mittler and Jones, 2024).

### 4.5. Transcriptional cascades and the disconnect from phenotypic resilience

Expression profiling of eleven targeted genes, specifically six heat tolerance transcripts (*HT1–HT6*) and five carbohydrate transport/biosynthesis genes (*SUC2*, *SUS3*, *SWEET10*, *ERD6L*, and

*PGTR1*), disclosed clear, cultivar-specific temporal profiles under thermal duress (Fig. 7). Crucially, the genotypes displaying the most intense transcript upregulation did not correspond to those exhibiting superior phenotypic tolerance, demonstrating a distinct uncoupling between stress signaling magnitude and actual physiological tolerance capacity.

The widespread prominence of midday transcript induction aligns with peak diurnal thermal loads and matches the known architecture of heat shock factor-regulated transcriptional regulation in grapevines (Liu et al., 2023; Hakeem et al., 2025). *HT1*, *HT2*, and *HT6* were most tightly induced at midday in Petit Verdot and Tempranillo, but shifted to a morning peak in Pinot Noir. Remarkably, Syrah maintained highly stable physiological performance despite lacking the highest transcriptional induction of these heat tolerance genes. This underscores that Syrah's climate resilience relies primarily on sustained constitutive stomatal and photosynthetic regulation, consistent with its open-stomatal anisohydric cooling capacity rather than acute, costly transcriptional activation.

Carbohydrate partitioning and sugar transport transcripts showed a complementary, variety-specific framework. *SUC2* and *SUS3* were strongly upregulated at midday in Petite Sirah and Syrah, respectively, whereas *SWEET10* and *ERD6L* peaked acutely in Petit Verdot and Tempranillo. The strong midday induction of *ERD6L* in Tempranillo matches its classification as a sensitive cultivar that relies heavily on dehydration-responsive pathways. These complementary transcripts demonstrate that sugar allocation and osmotic partitioning constitute a vital arm of grapevine heat adaptation, working in tandem with core chaperone proteins and transcription factor networks (Coupel-Ledru et al., 2024).

### 4.6. Topological architecture of integrated systems-level networks

Divergent topological structures across the grapevine networks reveal fundamentally distinct biological strategies under severe environmental anomalies. Syrah’s moderately dense, highly clustered network (density: 0.222; clustering: 0.773; 3 connected components) confirms that its field resilience is achieved through balanced, decentralized coordination across multiple metabolic pathways rather than reliance on a single protective mechanism (Fait et al., 2020; Reta et al., 2025). In contrast, Tempranillo’s elevated network heterogeneity (0.884) and elongated characteristic path length (2.359) mathematically represent a poorly coupled trait system, explaining its severe functional decline and high macro-canopy heat loading under peak stress conditions (Cardoso et al., 2022).

The consistent emergence of *HT1–HT6* and core sugar metabolism genes (*SWEET10*, *SUC2*, and *SUS3*) as system-wide hubs confirms that heat shock protection and carbohydrate partitioning form the invariant structural backbone of the grapevine stress response, regardless of a cultivar's baseline tolerance (Huang et al., 2022). Within this structure, *HT4* exhibited the highest composite VIP scores across all genotypes, indicating a highly conserved regulatory function that operates independently of genetic background (Fig. S7).

Crucially, the elevated betweenness centrality (>0.6) and high network stress values (>40,000) observed in *ERD6L* and *PGTR1* mathematically position these sugar transporters at the primary interface between central metabolism and downstream stress response modules. This topological bottleneck aligns with their diurnal expression patterns and explains the subsequent evening accumulation of free sugars, suggesting that transmembrane transport capacity is the rate-limiting step in post-stress recovery (Li and Zhao, 2024). These findings suggest that viticultural breeding programs aiming for heatwave resilience should target central nodes of transport and metabolic coordination rather than downstream stress-response genes (Grimplet et al., 2012).

## 5. Conclusions and future directions

Grapevine heatwave tolerance is governed by a coordinated network of physiological, metabolic, and transcriptional cascades. The successful identification of cultivar-specific tolerance strategies using ground-based parameters and UAV-based thermal imaging, coupled with a sparse predictive chemometric model that identified 10 primary metabolites, provides a method for classifying temporal stress responses. This minimized biomolecular and remote-sensing footprint offers a practical approach for high-throughput, rapid field screening of germplasm thermotolerance within viticultural breeding programs. Despite these insights, critical knowledge gaps remain. Comprehensive, untargeted transcriptomic profiling is necessary to validate these specific candidate hub pathways. Furthermore, these multi-scale mechanisms require validation across diverse macroclimatic regions, alongside long-term agronomic field trials to confirm whether the observed homeostatic traits translate into sustained, premium viticultural productivity and yield stability under seasonal shifts. Nevertheless, these results deliver foundational knowledge for precision viticulture pipelines that combine high-frequency aerial remote sensing with targeted molecular screening. Such frameworks are essential to maintaining crop production, fruit quality, and economic sustainability amid increasingly severe and recurrent summer heatwaves, and to enabling broader global applications of perennial crop climate-adaptation strategies.

Future research must evolve to merge radiometric thermal imagery with hyperspectral, LiDAR, and continuous environmental micro-sensors to capture structural and biochemical crop traits simultaneously. Longitudinal monitoring should also be expanded across distinct phenological stages and multi-year extreme weather anomalies. Finally, future workflows should prioritize the development of transferable artificial intelligence (AI) and machine learning models capable of robustly separating intrinsic genotypic response profiles from confounding effects of localized microclimates and vineyard management practices.

**Acknowledgments**

The authors are grateful to the Israeli Ministry of Agriculture and Rural Development for its financial support through the ERA-NET program (Project No. 5317) and the Goldinger Fund. We also express our sincere appreciation to The International Organisation of Vine and Wine (OIV) for its grant support for this study.

**Authorship contribution**

Kidanemaryam Reta: Writing – original draft, Writing – review & editing, Visualization, Validation, Software, Project administration, Methodology, Investigation, Formal analysis, Data curation, Conceptualization, Funding acquisition. Tamir Caras: Writing – review & editing, Methodology, Investigation. Pankaj Kumar Verma: Methodology, Investigation. Noga Sikron Persi: Methodology, Investigation. Nang Cherry: Investigation. Amnon Bustan: Conceptualization, Methodology, Writing – review & editing. Tarin Paz-Kagan: Supervision, Resources, Validation, Writing – review & editing. Naftali Lazarovitch: Writing – review & editing, Validation, Supervision, Resources, Project administration, Methodology, Funding acquisition, Conceptualization. Aaron Fait: Writing – review & editing, Validation, Supervision, Resources, Project administration, Methodology, Funding acquisition, Conceptualization.

**Declaration of Competing Interest**

The authors declare that they have no known competing financial interests or personal relationships that could have influenced the work reported in this paper.

## 6. Bibliography


Alahmad S., Smith D., Katsikis C., Aldiss Z., Brunner S.M., Meer S. V, et al. (2025). Phenotyping the hidden half: combining UAV phenotyping and machine learning to predict barley root traits in the field. *Journal of Experimental Botany*, Oxford University Press, Vol. 00 No. 0, pp. 1–18, doi: 10.1093/jxb/eraf268.

Araus J.L. and Cairns J.E. (2014). Field high-throughput phenotyping: The new crop breeding frontier. *Trends in Plant Science*, Vol. 19 No. 1, pp. 52–61, doi: 10.1016/j.tplants.2013.09.008.

Awais M., Li W., Cheema M.J.M., Zaman Q.U., Shaheen A., Aslam B., et al. (2023). UAV-based remote sensing in plant stress imagine using high-resolution thermal sensor for digital agriculture practices: a meta-review. *International Journal of Environmental Science and Technology*, Vol. 20 No. 1, pp. 1135–1152, doi: 10.1007/s13762-021-03801-5.

Bellvert J., Zarco-Tejada P.J., Girona J. and Fereres E. (2014). Mapping crop water stress index in a "Pinot-noir" vineyard: Comparing ground measurements with thermal remote sensing imagery from an unmanned aerial vehicle. *Precision Agriculture*, Vol. 15 No. 4, pp. 361–376, doi: 10.1007/s11119-013-9334-5.

Bernardo S., Dinis L.T., Machado N. and Moutinho-Pereira J. (2018). Grapevine abiotic stress assessment and search for sustainable adaptation strategies in Mediterranean-like climates. A review. *Agronomy for Sustainable Development 2018 38:6*, Springer, Vol. 38 No. 6, pp. 1–20, doi: 10.1007/S13593-018-0544-0.

Berry J. and Björkman O. (1980). Photosynthetic Response and Adaptation to Temperature in Higher Plants. *Annual Review of Plant Physiology*, Vol. 31 No. 1, pp. 491–543, doi: 10.1146/annurev.pp.31.060180.002423.

Bezdek J.C., Ehrlich R. and Full W. (1984). FCM: The fuzzy c-means clustering algorithm. *Computers & Geosciences*, Vol. 10 No. 2, pp. 191–203.

Botton A., Girardi F., Ruperti B., Brilli M., Tijero V., Eccher G., et al. (2022). Grape Berry Responses to Sequential Flooding and Heatwave Events: A Physiological, Transcriptional, and Metabolic Overview. *Plants*, Vol. 11 No. 3574, pp. 1–36, doi:

https://doi.org/10.3390/plants11243574.
Burchard-Levine V., Guerra J.G., Borra-Serrano I., Nieto H., Mesías-Ruiz G., Dorado J., et al. (2024). Evaluating the utility of combining high resolution thermal, multispectral and 3D imagery from unmanned aerial vehicles to monitor water stress in vineyards. *Precision Agriculture*, Springer US, Vol. 25 No. 5, pp. 2447–2476, doi: 10.1007/s11119-024-10179-0.
Burgess A.J. (2022). Wine without water: Improving grapevine tolerance to drought. *Plant Physiology*, Vol. 190 No. 3, pp. 1550–1551, doi: 10.1093/plphys/kiac381.
Caliński T. and Harabasz J. (1974). A dendrite method for cluster analysis. *Communications in Statistics*, Vol. 3 No. 1, pp. 1–27, doi: https://doi.org/10.1080/03610927408827101.
Cardoso L.L., Freire F.B.S. and Daloso D.M. (2022). Plant Metabolic Networks Under Stress: a Multi-species/Stress Condition Meta-analysis. *Journal of Soil Science and Plant Nutrition 2022*, Springer, Vol. 1, pp. 1–18, doi: 10.1007/S42729-022-01032-2.
Carvalho L.C., Coito J.L., Colaço S., Sangiogo M. and Amâncio S. (2015). Heat stress in grapevine: The pros and cons of acclimation. *Plant Cell and Environment*, Vol. 38 No. 4, pp. 777–789, doi: 10.1111/pce.12445.
Ćavar Zeljković S., Saeed F., Šamec D. and Chaudhry U.K. (2026). Methodological Advances in Transcriptomics and Metabolomics for Assessing Crop Stress Resilience. *Physiologia Plantarum*, Vol. 178 No. 1, doi: 10.1111/ppl.70717.
Cembrowska-Lech D., Krzemińska A., Miller T., Nowakowska A., Adamski C., Radaczyńska M., et al. (2023). An Integrated Multi-Omics and Artificial Intelligence Framework for Advance Plant Phenotyping in Horticulture. *Biology*, Vol. 12 No. 10, doi: 10.3390/biology12101298.
Coupel-Ledru A., Westgeest A.J., Albasha R., Millan M., Pallas B., Doligez A., et al. (2024). Clusters of grapevine genes for a burning world. *New Phytologist*, Vol. 242 No. 1, pp. 10–18, doi: 10.1111/nph.19540.
Dai Z.W., Ollat N., Gomès E., Decroocq S., Tandonnet J.P., Bordenave L., et al. (2011). Ecophysiological, Genetic, and Molecular Causes of Variation in Grape Berry Weight and Composition: A Review. *American Journal of Enology and Viticulture*, American Journal of Enology and Viticulture, Vol. 62 No. 4, pp. 413–425, doi: 10.5344/AJEV.2011.10116.
Degu A., Hochberg U., Sikron N., Venturini L., Buson G., Ghan R., et al. (2014). Metabolite and transcript profiling of berry skin during fruit development elucidates differential regulation between Cabernet Sauvignon and Shiraz cultivars at branching points in the polyphenol pathway. *BMC Plant Biology*, Vol. 14 No. 1, pp. 1–20, doi: 10.1186/s12870-014-0188-4.
Dou F., Phillip F.O., Liu G., Zhu J., Zhang L., Wang Y., et al. (2024). Transcriptomic and physiological analyses reveal different grape varieties response to high temperature stress. *Frontiers in Plant Science*, Vol. 15 No. March, pp. 1–18, doi: 10.3389/fpls.2024.1313832.
Fahlgren N., Gehan M.A. and Baxter I. (2015). Lights, camera, action: High-throughput plant phenotyping is ready for a close-up. *Current Opinion in Plant Biology*, Elsevier Ltd, Vol. 24, pp. 93–99, doi: 10.1016/j.pbi.2015.02.006.
Fait A., Batushansky A., Shrestha V., Yobi A. and Angelovici R. (2020). Can metabolic tightening and expansion of co-expression network play a role in stress response and tolerance? *Plant Science*, Elsevier, Vol. 293 No. 110409, doi: 10.1016/j.plantsci.2020.110409.
FAOSTAT. (2023). Crops and livestock products statistic. *FAO*, available at: https://www.fao.org/faostat/en/#data/QCL/visualize (accessed 19 January 2025).
Faralli M., Bontempo L., Bianchedi P.L., Moser C., Bertamini M., Lawson T., et al. (2022). Natural variation in stomatal dynamics drives divergence in heat stress tolerance and contributes to seasonal intrinsic water-use efficiency in Vitis vinifera (subsp. sativa and

sylvestris). *Journal of Experimental Botany*, Vol. 73 No. 10, pp. 3238–3250, doi: 10.1093/jxb/erab552.

Flexas J., Galmés J., Gallé A., Gulías J., Pou A., Ribas-Carbo M., et al. (2010). Improving water use efficiency in grapevines: Potential physiological targets for biotechnological improvement. *Australian Journal of Grape and Wine Research*, Vol. 16, pp. 106–121, doi: 10.1111/j.1755-0238.2009.00057.x.

Gago J., Fernie A.R., Nikoloski Z., Tohge T., Martorell S., Escalona J.M., et al. (2017). Integrative field scale phenotyping for investigating metabolic components of water stress within a vineyard. *Plant Methods*, BioMed Central, Vol. 13 No. 1, pp. 1–14, doi: 10.1186/s13007-017-0241-z.

Gambetta G.A., Herrera J.C., Dayer S., Feng Q., Hochberg U. and Castellarin S.D. (2020). The physiology of drought stress in grapevine: towards an integrative definition of drought tolerance. *Journal of Experimental Botany*, J Exp Bot, Vol. 71 No. 16, pp. 4658–4676, doi: 10.1093/jxb/eraa245.

Gambetta J.M., Holzapfel B.P., Stoll M. and Friedel M. (2021). Sunburn in Grapes: A Review. *Frontiers in Plant Science*, Frontiers Media S.A., Vol. 11, p. 2123, doi: 10.3389/fpls.2020.604691.

Gambino G., Perrone I. and Gribaudo I. (2008). A rapid and effective method for RNA extraction from different tissues of grapevine and other woody plants. *Phytochemical Analysis*, John Wiley and Sons Ltd, Vol. 19 No. 6, pp. 520–525, doi: 10.1002/pca.1078.

Garcia-Garcia D., Reynafarje la Rosa X., Grados Bedoya D. and Schrevens E. (2021). Linear mixed model analysis of NDVI-based canopy coverage, extracted from sequential UAV multispectral imagery of an open field tomato irrigation experiment. *Computers and Electronics in Agriculture*, Elsevier B.V., Vol. 189, p. 106399, doi: 10.1016/j.compag.2021.106399.

Gashu K., Sikron Persi N., Drori E., Harcavi E., Agam N., Bustan A., et al. (2020). Temperature Shift Between Vineyards Modulates Berry Phenology and Primary Metabolism in a Varietal Collection of Wine Grapevine. *Frontiers in Plant Science*, Vol. 11, pp. 1–23, doi: 10.3389/fpls.2020.588739.

Gashu K., Song C., Dubey A.K., Acuña T., Sagi M., Agam N., et al. (2022). The Effect of Topo-Climate Variation on the Secondary Metabolism of Berries in White Grapevine Varieties (Vitis vinifera). *Frontiers in Plant Science*, Frontiers Media S.A., Vol. 13, p. 487, doi: 10.3389/fpls.2022.847268.

Ghosh U.K., Islam M.N., Siddiqui M.N. and Khan M.A.R. (2021). Understanding the roles of osmolytes for acclimatizing plants to changing environment: a review of potential mechanism. *Plant Signaling and Behavior*, Taylor & Francis, Vol. 16 No. 8, doi: 10.1080/15592324.2021.1913306.

Greer D.H. (2024). Intraspecific differences in the photosynthetic responses to chloroplast CO2 and photon flux density at different leaf temperatures of four grapevine cultivars grown in common outdoor conditions. *Plant Direct*, Vol. 8 No. 6, pp. 1–16, doi: 10.1002/pld3.595.

Greer D.H. and Weedon M.M. (2012). Modelling photosynthetic responses to temperature of grapevine (Vitis vinifera cv. Semillon) leaves on vines grown in a hot climate. *Plant, Cell and Environment*, Vol. 35 No. 6, pp. 1050–1064, doi: 10.1111/j.1365-3040.2011.02471.x.

Grimplet J., Van Hemert J., Carbonell-Bejerano P., Díaz-Riquelme J., Dickerson J., Fennell A., et al. (2012). Comparative analysis of grapevine whole-genome gene predictions, functional annotation, categorization and integration of the predicted gene sequences. *BMC Research*

*Notes*, Vol. 5 No. 213, doi: 10.1186/1756-0500-5-213.
Gu Z. (2022). Complex heatmap visualization. *IMeta*, Vol. 1 No. 3, pp. 1–15, doi: 10.1002/imt2.43.
Gu Z., Eils R. and Schlesner M. (2016). Complex heatmaps reveal patterns and correlations in multidimensional genomic data. *Bioinformatics*, Oxford Academic, Vol. 32 No. 18, pp. 2847–2849, doi: 10.1093/BIOINFORMATICS/BTW313.
Guo M., Liu J.H., Ma X., Luo D.X., Gong Z.H. and Lu M.H. (2016). The plant heat stress transcription factors (HSFS): Structure, regulation, and function in response to abiotic stresses. *Frontiers in Plant Science*, Vol. 7, doi: 10.3389/fpls.2016.00114.
Guo R., Shi L.X., Yan C., Zhong X., Gu F.X., Liu Q., et al. (2017). Ionomic and metabolic responses to neutral salt or alkaline salt stresses in maize (Zea mays L.) seedlings. *BMC Plant Biology*, BMC Plant Biology, Vol. 17 No. 1, pp. 1–13, doi: 10.1186/s12870-017-0994-6.
Guo Y., Li S., García-Caparros P., Wang L. and Liang Z. (2025). Grapevine adaptation to cold and heat stress. *Journal of Experimental Botany*, Vol. 76 No. 11, pp. 3038–3058, doi: https://doi.org/10.1093/jxb/eraf158.
Hakeem A., Li S., Iqbal S., Elatafi E., Badar R., Emmie A., et al. (2025). Effects of salt stress on growth , physio - biochemical traits , and tolerance mechanism of grapevine rootstocks. *Euphytica*, Springer Netherlands, Vol. 221, doi: https://doi.org/10.1007/s10681-025-03574-9.
Havaux M. (1998). Carotenoids as membrane stabilizers in chloroplasts. *Trends in Plant Science*, Vol. 3 No. 4, pp. 147–151, doi: 10.1016/S1360-1385(98)01200-X.
Hewitt S., Hernández-Montes E., Dhingra A. and Keller M. (2023). Impact of heat stress, water stress, and their combined effects on the metabolism and transcriptome of grape berries. *Scientific Reports*, natureportfolio, Vol. 13 No. 1, pp. 1–14, doi: 10.1038/s41598-023-36160-x.
Hochberg U., Degu A., Toubiana D., Gendler T., Nikoloski Z., Rachmilevitch S., et al. (2013). Metabolite profiling and network analysis reveal coordinated changes in grapevine water stress response. *BMC Plant Biology*, BioMed Central, Vol. 13 No. 1, pp. 1–16, doi: 10.1186/1471-2229-13-184.
Huang L.Z., Zhou M., Ding Y.F. and Zhu C. (2022). Gene Networks Involved in Plant Heat Stress Response and Tolerance. *International Journal of Molecular Sciences*, Vol. 23 No. 19, doi: 10.3390/ijms231911970.
IPCC. (2023). *Section 4: Near-Term Responses in a Changing Climate*. *Climate Change 2023: Synthesis Report*, doi: 10.59327/IPCC/AR6-9789291691647.
Kassambara A. and Mundt F. (2020). factoextra: Extract and Visualize the Results of Multivariate Data Analyses.
Katimbo A., Rudnick D.R., DeJonge K.C., Lo T.H., Qiao X., Franz T.E., et al. (2022). Crop water stress index computation approaches and their sensitivity to soil water dynamics. *Agricultural Water Management*, Elsevier B.V., Vol. 266, p. 107575, doi: 10.1016/j.agwat.2022.107575.
Kotak S., Larkindale J., Lee U., von Koskull-Döring P., Vierling E. and Scharf K.D. (2007). Complexity of the heat stress response in plants. *Current Opinion in Plant Biology*, Vol. 10 No. 3, pp. 310–316, doi: 10.1016/j.pbi.2007.04.011.
Krasensky J. and Jonak C. (2012). Drought, salt, and temperature stress-induced metabolic rearrangements and regulatory networks. *Journal of Experimental Botany*, Vol. 63 No. 4, pp. 1593–1608, doi: 10.1093/jxb/err460.
Kundu S., Saini D.K., Meena R.K., Bahuguna R.N. and Jagadish S.V.K. (2024). High-throughput

phenotyping and AI technologies for deciphering crop resilience to heat stress. *Plant Physiology Reports*, Vol. 29 No. 4, pp. 699–715, doi: 10.1007/s40502-024-00821-4.

Lauterberg M., Tschiersch H., Zhao Y., Kuhlmann M., Mücke I., Papa R., et al. (2024). Implementation of theoretical non-photochemical quenching (NPQ(T)) to investigate NPQ of chickpea under drought stress with High-throughput Phenotyping. *Scientific Reports*, Nature Publishing Group UK, Vol. 14 No. 1, pp. 1–12, doi: 10.1038/s41598-024-63372-6.

van Leeuwen C., Sgubin G., Bois B., Ollat N., Swingedouw D., Zito S., et al. (2024). Climate change impacts and adaptations of wine production. *Nature Reviews Earth & Environment*, Nature Publishing Group, Vol. 5 No. 4, pp. 258–275, doi: 10.1038/s43017-024-00521-5.

Li G. and Zhao Y. (2024). The critical roles of three sugar-related proteins (HXK, SnRK1, TOR) in regulating plant growth and stress responses. *Horticulture Research*, Vol. 11 No. 6, doi: 10.1093/hr/uhae099.

Liang X., Yu S., Ju Y., Wang Y. and Yin D. (2025). Multi-Scale Remote-Sensing Phenomics Integrated with Multi-Omics: Advances in Crop Drought–Heat Stress Tolerance Mechanisms and Perspectives for Climate-Smart Agriculture. *Plants*, Vol. 14 No. 18, pp. 1–34, doi: 10.3390/plants14182829.

Lisec J., Schauer N., Kopka J., Willmitzer L. and Fernie A.R. (2006). Gas chromatography mass spectrometry-based metabolite profiling in plants. *Nature Protocols*, Vol. 1 No. 1, pp. 387–396, doi: 10.1038/nprot.2006.59.

Liu X., Chen H., Li S., Lecourieux D., Duan W., Fan P., et al. (2023). Natural variations of HSFA2 enhance thermotolerance in grapevine. *Horticulture Research*, Vol. 10 No. 1, doi: 10.1093/hr/uhac250.

Marchin R.M., Backes D., Ossola A., Leishman M.R., Tjoelker M.G. and Ellsworth D.S. (2022). Extreme heat increases stomatal conductance and drought-induced mortality risk in vulnerable plant species. *Global Change Biology*, Vol. 28 No. 3, pp. 1133–1146, doi: 10.1111/gcb.15976.

Martínez-Lüscher J., Matus J.T., Gomès E. and Pascual I. (2025). Toward understanding grapevine responses to climate change: A multi-stress and holistic approach. *Journal of Experimental Botany*, Vol. 76 No. 11, pp. 2949–2969, doi: 10.1093/jxb/erae482.

Mathur S., Agrawal D. and Jajoo A. (2014). Photosynthesis: Response to high temperature stress. *Journal of Photochemistry and Photobiology B: Biology*, Elsevier B.V., Vol. 137, pp. 116–126, doi: 10.1016/j.jphotobiol.2014.01.010.

Maxwell K. and Johnson G.N. (2000). Chlorophyll fluorescence—a practical guide. *Journal of Experimental Botany*, Oxford Academic, Vol. 51 No. 345, pp. 659–668, doi: 10.1093/JEXBOT/51.345.659.

Medrano H., Escalona J.M., Bota J., Gulías J. and Flexas J. (2002). Regulation of photosynthesis of C3 plants in response to progressive drought: Stomatal conductance as a reference parameter. *Annals of Botany*, Vol. 89, pp. 895–905, doi: 10.1093/aob/mcf079.

Mittler R., Finka A. and Goloubinoff P. (2012). How do plants feel the heat? *Trends in Biochemical Sciences*, Elsevier Ltd, Vol. 37 No. 3, pp. 118–125, doi: 10.1016/j.tibs.2011.11.007.

Mittler R. and Jones D.P. (2024). The redox code of plants. *Plant Cell and Environment*, Vol. 47 No. 8, pp. 2821–2829, doi: 10.1111/pce.14787.

Mozell M.R. and Thach L. (2014). The impact of climate change on the global wine industry: Challenges & solutions. *Wine Economics and Policy*, Vol. 3 No. 2, pp. 81–89, doi: 10.1016/j.wep.2014.08.001.

Nayak L., Lal M.K., Tiwari R.K., Kumar R., Lal P., Das R., et al. (2023). A balancing act: Exploring the interplay between HSPs and osmoprotectants in temperature stress responses. *South African Journal of Botany*, Elsevier B.V., Vol. 162, pp. 64–71, doi: 10.1016/j.sajb.2023.08.069.

Neri P., Gu L. and Song Y. (2024). The effect of temperature on photosystem II efficiency across plant functional types and climate. *Biogeosciences*, Vol. 21 No. 11, pp. 2731–2758, doi: 10.5194/bg-21-2731-2024.

Obata T. and Fernie A.R. (2012). The use of metabolomics to dissect plant responses to abiotic stresses. *Cellular and Molecular Life Sciences*, Springer, Vol. 69 No. 19, pp. 3225–3243, doi: 10.1007/s00018-012-1091-5.

OIV. (2023). *State of the World Vine and Wine Sector*. *International Organisation of Vine and Wine*.

OIV. (2025). *World Wine Production Outlook 2025*. *International Organization of Vine and Wine (OIV)*.

Pastore C., Santo S.D., Zenoni S., Movahed N., Allegro G., Valentini G., et al. (2017). Whole plant temperature manipulation affects flavonoid metabolism and the transcriptome of grapevine berries. *Frontiers in Plant Science*, Frontiers Media S.A., Vol. 8, p. 929, doi: 10.3389/fpls.2017.00929.

Pettenuzzo S., Cappellin L., Grando M.S. and Costantini L. (2022). Phenotyping methods to assess heat stress resilience in grapevine. *Journal of Experimental Botany*, Vol. 73 No. 15, pp. 5128–5148, doi: 10.1093/jxb/erac058.

Posit team. (2025). RStudio: Integrated Development Environment for R., Posit Software,PBC, Boston, MA.

QGIS Development Team. (2021). QGIS Geographic Information System, QGIS Association, Białowieża.

Qiu Q., Sun Y., Guo D., Wang L., Pagay V. and Wang S. (2025). Heat Stress Downregulates Photosystem I Redox State on Leaf Photosynthesis in Grapevine. *Agronomy*, Vol. 15 No. 4, doi: 10.3390/agronomy15040948.

R Core Team. (2024). R: A language and environment for statistical computing, R Foundation for Statistical Computing, Vienna, Austria.

R Core Team. (2025). R: A language and environment for statistical computing. R Foundation for Statistical Computing, Vienna, Austria.

Reta K., Lazarovitch N. and Fait A. (2025). Metabolic and physiological analysis reveals distinct salinity tipping point in Vitis vinifera cv. Syrah to enter a stress response mode. *Plant Stress*, Elsevier B.V., Vol. 16, pp. 1–14, doi: 10.1016/j.stress.2025.100864.

Reta K., Lupo Y., Sikron-Persi N., Acuña T., Lazarovitch N. and Fait A. (2026). Metabolic network tightening and antagonistic stress interactions drive rootstock-mediated tolerance to combined salinity and water-deficit stress in grapevine cv.Syrah. *Plant Stress*, Elsevier, p. 101456, doi: 10.1016/J.STRESS.2026.101456.

Revelle W. (2023). psych: Procedures for Psychological, Psychometric, and Personality Research, Northwestern University, Evanston, Illinois.

Rienth M., Torregrosa L., Sarah G., Ardisson M., Brillouet J.M. and Romieu C. (2016). Temperature desynchronizes sugar and organic acid metabolism in ripening grapevine fruits and remodels their transcriptome. *BMC Plant Biology*, BMC Plant Biology, Vol. 16 No. 1, pp. 1–23, doi: 10.1186/s12870-016-0850-0.

Rogiers S.Y., Greer D.H., Hatfield J.M., Hutton R.J., Clarke S.J., Hutchinson P.A., et al. (2012).

Stomatal response of an anisohydric grapevine cultivar to evaporative demand, available soil moisture and abscisic acid. *Tree Physiology*, Vol. 32 No. 3, pp. 249–261, doi: 10.1093/treephys/tpr131.

Rohart F., Gautier B., Singh A. and Cao K.-A.L. (2017). mixOmics: An R package for 'omics feature selection and multiple data integration. *PLoS Computational Biology*, Vol. 13 No. 11, pp. 1–14, doi: 10.1371/journal.pcbi.1005752.

Sadras V.O., Montoro A., Moran M.A. and Aphalo P.J. (2012). Elevated temperature altered the reaction norms of stomatal conductance in field-grown grapevine. *Agricultural and Forest Meteorology*, Elsevier B.V., Vol. 165, pp. 35–42, doi: 10.1016/j.agrformet.2012.06.005.

Salvi P., Kamble N.U. and Majee M. (2018). Stress-Inducible Galactinol Synthase of Chickpea (CaGolS) is Implicated in Heat and Oxidative Stress Tolerance through Reducing Stress-Induced Excessive Reactive Oxygen Species Accumulation. *Plant and Cell Physiology*, Vol. 59 No. 1, pp. 155–166, doi: 10.1093/pcp/pcx170.

Salvucci M.E. and Crafts-Brandner S.J. (2004). Inhibition of photosynthesis by heat stress: The activation state of Rubisco as a limiting factor in photosynthesis. *Physiologia Plantarum*, Vol. 120 No. 2, pp. 179–186, doi: 10.1111/j.0031-9317.2004.0173.x.

Shannon P., Markiel A., Ozier O., Baliga N.S., Wang J.T., Ramage D., et al. (2003). Cytoscape: A Software Environment for Integrated Models of Biomolecular Interaction Networks. *Genome Research*, Vol. 13 No. 11, pp. 2498–2504, doi: 10.1101/gr.1239303.

Sharma K., Bhatt U. and Soni V. (2026). Artificial Intelligence-Assisted Detection of Abiotic Stress in Agricultural Crops: Sensors, Computational Models, and Outlook. *Journal of Crop Health*, Vol. 78 No. 3, doi: 10.1007/s10343-026-01334-w.

Tardieu F., Cabrera-Bosquet L., Pridmore T. and Bennett M. (2017). Plant Phenomics, From Sensors to Knowledge. *Current Biology*, Vol. 27 No. 15, pp. R770–R783, doi: 10.1016/j.cub.2017.05.055.

Tian M.B., Lu H.C., Shi N., Li M.Y., Wei J.Y., Deng J.Y., et al. (2025). Afternoon shading delays ripening and modifies grape flavonoids and wine composition under natural heat stress in semi-arid regions. *Food Chemistry: X*, Elsevier Ltd, Vol. 29 No. July, p. 102831, doi: 10.1016/j.fochx.2025.102831.

Tombesi S., Nardini A., Frioni T., Soccolini M., Zadra C., Farinelli D., et al. (2015). Stomatal closure is induced by hydraulic signals and maintained by ABA in drought-stressed grapevine. *Scientific Reports*, Nature Publishing Group, Vol. 5 No. June, pp. 1–12, doi: 10.1038/srep12449.

Torregrosa L., Bigard A., Doligez A., Lecourieux D., Rienth M., Luchaire N., et al. (2017). Developmental, molecular and genetic studies on grapevine response to temperature open breeding strategies for adaptation to warming. *Oeno One*, Vol. 51 No. 2, pp. 155–165, doi: 10.20870/oeno-one.2016.0.0.1587.

Treier S., Roth L., Hund A., Aasen H., Levy Häner L., Vuille-dit-Bille N., et al. (2025). Analysis of variance and its sources in UAV-based multi-view thermal imaging of wheat plots. *Plant Phenomics*, Elsevier, Vol. 7 No. 2, doi: 10.1016/j.plaphe.2025.100046.

Venios X., Korkas E., Nisiotou A. and Banilas G. (2020). Grapevine responses to heat stress and global warming. *Plants*, Vol. 9 No. 12, pp. 1–15, doi: 10.3390/plants9121754.

Villano C., Aiese Cigliano R., Esposito S., D'Amelia V., Iovene M., Carputo D., et al. (2022). DNA-Based Technologies for Grapevine Biodiversity Exploitation: State of the Art and Future Perspectives. *Agronomy*, Vol. 12 No. 2, pp. 1–16, doi: 10.3390/agronomy12020491.

Wegher M., Niedrist G., Tagliavini M., Asensio D., Giuliani N. and Andreotti C. (2025). Impact

of leaf removal on recovery of young grapevines under heatwave conditions : A study in an ecotron environment. *OENO One*, Vol. 59 No. 3, pp. 1–14.

Werner C., Fasbender L., Romek K.M., Yáñez-Serrano A.M. and Kreuzwieser J. (2020). Heat Waves Change Plant Carbon Allocation Among Primary and Secondary Metabolism Altering CO2 Assimilation, Respiration, and VOC Emissions. *Frontiers in Plant Science*, Vol. 11, pp. 1–17, doi: 10.3389/fpls.2020.01242.

Wickham H. (2016). *Ggplot2: Elegant Graphics for Data Analysis. Springer-Verlag New York*. Vol. 35.

Wilson A., Dizy M., Dominguez D., de Rosas M.I., Baldo Y., Garcia L., et al. (2024). Overhead spray water treatment as a mitigation strategy to alleviate vine stress and safeguard grape quality during heatwaves. *Oeno One*, Vol. 58 No. 2, doi: 10.20870/oeno-one.2024.58.2.7847.

Wolkovich E.M., García De Cortázar-Atauri I., Morales-Castilla I., Nicholas K.A. and Lacombe T. (2018). From Pinot to Xinomavro in the world's future wine-growing regions. *Nature Climate Change*, Springer US, Vol. 8 No. 1, pp. 29–37, doi: 10.1038/s41558-017-0016-6.

Ye J., Coulouris G., Zaretskaya I., Cutcutache I., Rozen S. and Madden T.L. (2012). Primer-BLAST: A tool to design target-specific primers for polymerase chain reaction. *BMC Bioinformatics*, Vol. 13 No. 134.

Zarco-Tejada P.J., Guillén-Climent M.L., Hernández-Clemente R., Catalina A., González M.R. and Martín P. (2013). Estimating leaf carotenoid content in vineyards using high resolution hyperspectral imagery acquired from an unmanned aerial vehicle (UAV). *Agricultural and Forest Meteorology*, Elsevier B.V., Vol. 171–172, pp. 281–294, doi: 10.1016/j.agrformet.2012.12.013.

Zhao J., He Q., Chen G., Wang L. and Jin B. (2016). Regulation of non-coding RNAs in heat stress responses of plants. *Frontiers in Plant Science*, Vol. 7, pp. 1–9, doi: 10.3389/fpls.2016.01213.

Zuo G. (2025). Non-photochemical quenching (NPQ) in photoprotection: insights into NPQ levels required to avoid photoinactivation and photoinhibition. *New Phytologist*, Vol. 246 No. 5, pp. 1967–1974, doi: 10.1111/nph.70121.

## 7. Supplementary File

Supplementary Tables

Table S.1: Summary of temperature distributions across Fuzzy C-Means (FCM) clusters across three sampling times in two years. The numbers represent the temperature differences (Δ) calculated from the temperatures measured during three flights (Morning, Noon, and Evening) in the two years. The table presents the mean difference ± standard deviation, and the letters indicate significant differences. In both years and in both Morning-Noon and Noon-Evening (all cases), differences are significant.

| Year | Cluster | Morning-Noon | Noon-Evening |
|---|---|---|---|
| 2022 | Cluster 1 | 8.14±0.20(a) | -3.50±0.31(a) |
| | Cluster 2 | 6.01±0.32(b) | -1.45±0.31(b) |
| 2023 | Cluster 1 | 7.70±0.33(a) | -4.86±0.21(a) |
| | Cluster 2 | 3.77±0.27(b) | -3.13±0.39(b) |

Table S.2: Summary of individual plant-based FCM clustering showing the number of plants that fall into which cluster based on the canopy temperature difference during the day, as a difference calculated from morning to noon as heating up, and from noon to evening as recovery/cooling down.

| Year | Cluster | Petite Sirah | Petit Verdot | Pinot Noir | Sangiovese | Syrah | Tempranillo |
|---|---|---|---|---|---|---|---|
| 2022 | Cluster 1 | 1 | 2 | 1 | 2 | 4 | 1 |
| | Cluster 2 | 3 | 2 | 3 | 2 | 0 | 3 |
| 2023 | Cluster 1 | 1 | 1 | 2 | 0 | 2 | 2 |
| | Cluster 2 | 3 | 3 | 2 | 4 | 2 | 2 |

Supplementary Figures

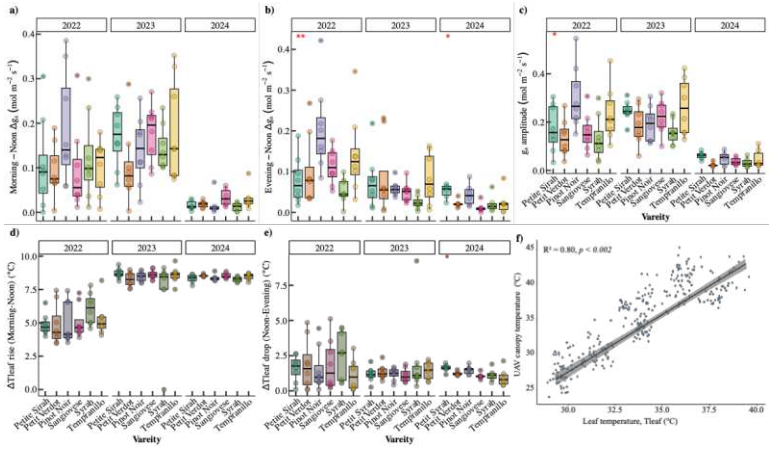



Figure S. 1: Stomatal conductance ($g_s$) and Leaf temperature changes between time points. Delta stomatal conductance ($\Delta g_s$) refers to the difference between two timepoints: Morning to noon (a), Evening to Noon (b), and gs amplitude during the day (c). Delta for leaf temperature measurements obtained using the LI-6800 portable photosynthesis system: Tleaf rise from Morning to Noon (d) and Tleaf drop from Noon to Evening (e). Asterisks in panels indicate significant differences between varieties (red) ($p < 0.05$).

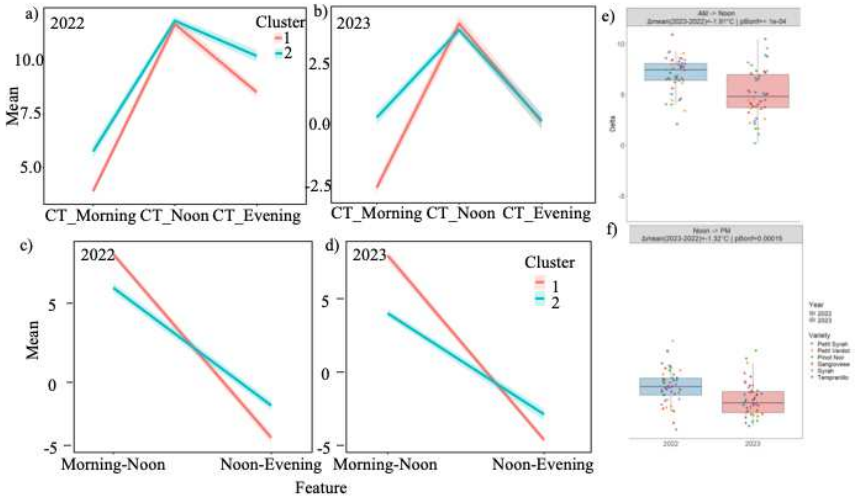



Figure S. 2: Longitudinal trajectory profiles of two identified clusters across time points.
Mean trajectories for Cluster 1 (red) and Cluster 2 (teal) in 2022 (a) and 2023 (b), with shaded regions representing 95% confidence intervals. Both clusters exhibit an initial increase followed by a decline across morning, noon, and evening time points. Mean differences in trajectories between clusters from Morning to Noon and from Noon to Evening in 2022 (c) and 2023 (d). Both clusters follow a monotonically decreasing trend across the day. Cluster assignments were determined using the fuzzy clustering method. Temperature delta comparisons between years (2022 and 2023) for the Morning to Noon (e) and Noon to Evening (f), showing significant changes. Boxplots show the distribution of delta values per year, with individual data points overlaid and colored by grape variety. Δmean and bootstrapped p-values are indicated as adjusted Bonf values.

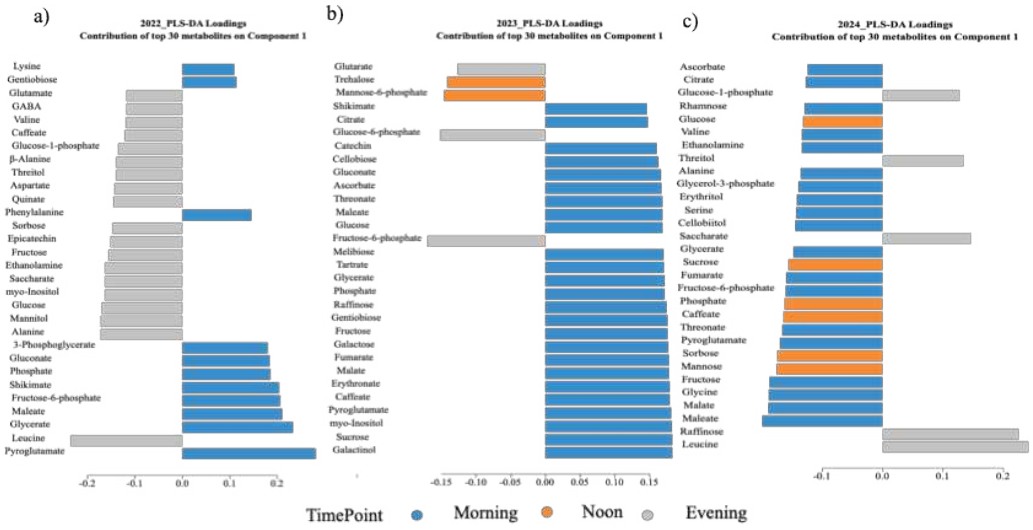



Figure S. 3: PLS-DA loading plots of central metabolites in each growing season across timepoints: (a) 2022, (b) 2023, and (c) 2024.

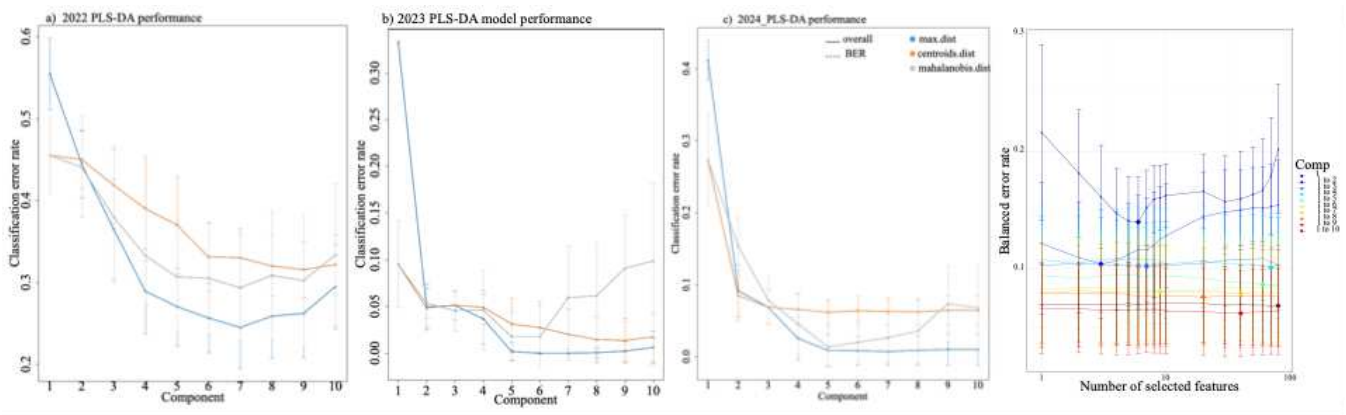



Figure S. 4: Classification error rates plotted against feature dimensions (PLS-DA components) using linear discriminant functions as a model performance indicator, (a) 2022, (b) 2023, and (c) 2024. Error rates decrease with increasing component number until optimal model complexity is reached. Feature selection tuning for PLS-DA using the mixOmics package, showing balanced error rates as a function of the number of features (d). The plot displays 10-fold cross-validation results across different feature subset sizes, with optimal feature selection (n = 10 features) identified at a minimum balanced error rate of <15% for the first component.

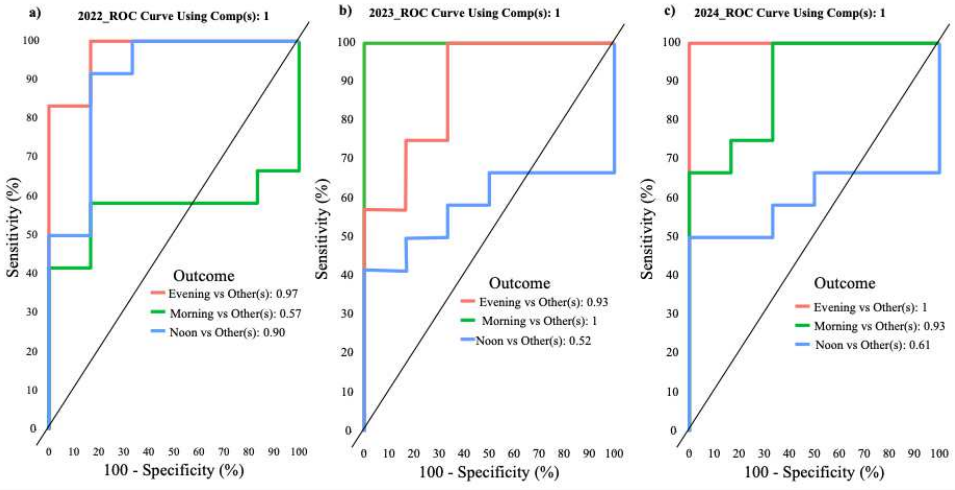



Figure S. 5: ROC curves of varieties for each timepoint (a) 2022, (b) 2023, and (c) 2024 illustrate the predictive performance of metabolic turnover indicators in identifying severe stress under heatwave across the day on heatwave events.

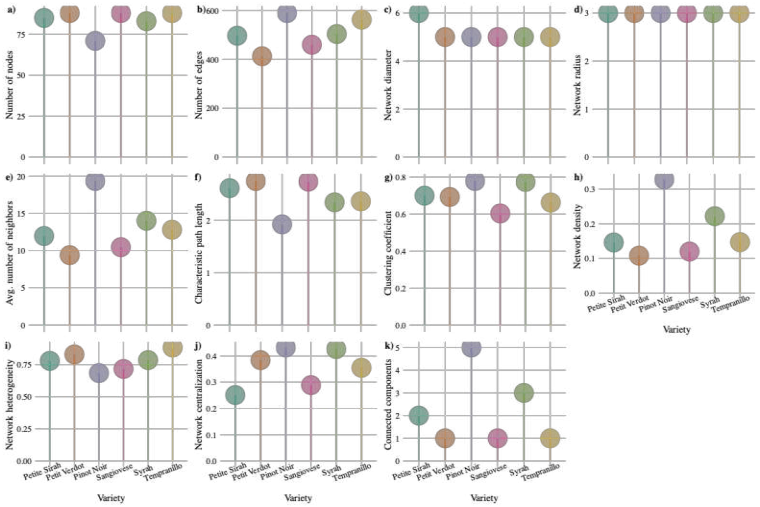



Figure S. 6: Comprehensive topological analysis of correlation-based metabolic networks across six grape varieties. Global network properties: (a) number of nodes, (b) number of edges, (c) network diameter, (d) network radius, (e) average number of neighbors, (f) characteristic path length, (g) clustering coefficient, (h) network density, (i) network heterogeneity, (j) network centralization, and (k) connected components. These structural metrics collectively characterize the organizational complexity, connectivity patterns, and topological architecture of variety-specific metabolic networks under heat stress conditions. Each variety is distinguished by color coding.

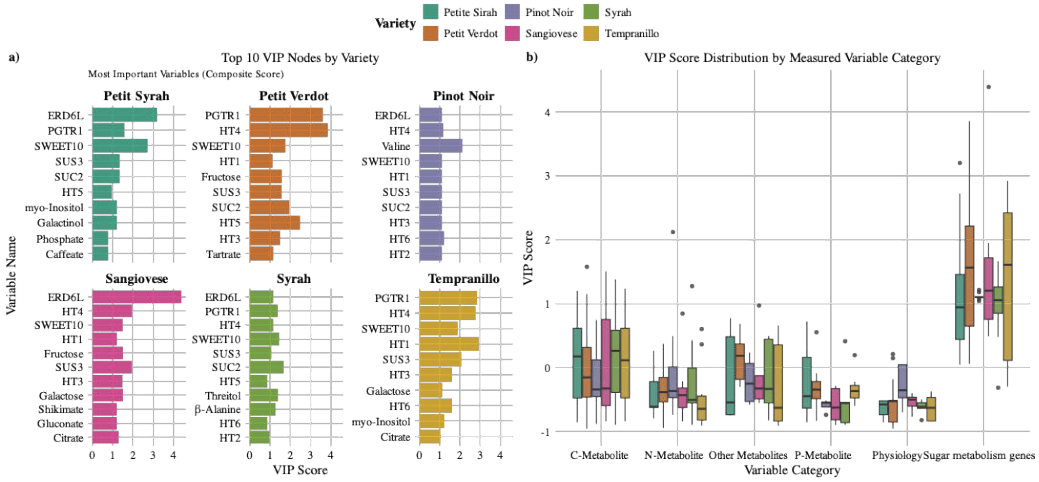



Figure S. 7: Variable Importance in Projection (VIP) analysis of correlation-based metabolic networks across grape varieties. (a) Top 10 VIP nodes ranked by composite importance score for each variety, showing the most critical metabolites, genes, and physiological traits based on normalized centrality measures (degree, betweenness centrality, closeness centrality, and stress centrality). (b) Distribution of VIP scores across different variable categories (metabolites, thermal measurements, sugar metabolism genes, and physiological traits) for each grape variety, with varieties distinguished by color coding. VIP scores represent the relative importance of each node within the network topology, identifying key regulatory hubs and bottleneck components in variety-specific stress response networks. Higher VIP scores indicate nodes that are simultaneously well-connected, centrally positioned, and critical for maintaining network connectivity and information flow.